bioRxiv preprint doi: https://doi.org/10.1101/2023.10.13.562210; this version posted October 17, 2023. The copyright holder for this preprint (which was not certified by peer review) is the author/funder, who has granted bioRxiv a license to display the preprint in perpetuity. It is made available under a CC-BY-NC-ND 4.0 International license.

Transformation of neural coding for vibrotactile stimuli along the ascending somatosensory pathway

Authors: Kuo-Sheng Lee[1]*, Alastair Loutit[1], Dominica de Thomas Wagner[1], Mark Sanders[1], Mario Prsa[2], Daniel Huber[1]*

Affiliations:

[1]Department of Basic Neurosciences, University of Geneva, Geneva, Switzerland

[2]Department of Neuroscience and Movement Science, University of Fribourg, Fribourg, Switzerland

*Corresponding author: Kuo-Sheng.Lee@unige.ch and Daniel.Huber@unige.ch.

Abstract: Perceiving substrate vibrations is a fundamental component of somatosensation. In mammals, action potentials fired by rapidly adapting mechanosensitive afferents are known to reliably time lock to the cycles of a vibration. This stands in contrast to coding in the higher-order somatosensory cortices, where neurons generally encode vibrations in their firing rates, which are tuned to a preferred vibration frequency. How and where along the ascending neuraxis is the peripheral afferent temporal code of cyclically entrained action potentials transformed into a rate code is currently not clear. To answer this question, we probed the encoding of vibrotactile stimuli with electrophysiological recordings along all stages of the ascending somatosensory pathway in mice. Recordings from individual primary sensory neurons in lightly anesthetized mice revealed that rapidly adapting mechanosensitive afferents innervating Pacinian corpuscles display phase-locked spiking for vibrations up to 2000 Hz. This precise temporal code was reliably preserved through the brainstem dorsal column nuclei. The main transformation step was identified at the level of the thalamus, where we observed a significant loss of phase-locked spike timing information accompanied by a further narrowing of the width of the tuning curves. Using optogenetic manipulation of thalamic inhibitory circuits, we found that parvalbumin-positive interneurons in thalamic reticular nucleus participate in sharpening the frequency selectivity and disrupting the precise spike timing of ascending neural signals encoding vibrotactile stimuli. To test the functional implications of these different neural coding mechanisms, we applied frequency-specific microstimulation within the brainstem and demonstrated that they can drive the frequency selectivity in the somatosensory cortex reminiscent of the actual response to vibration, whereas microstimulation within thalamus cannot. Finally, we applied microstimulation in the brainstem of behaving mice and demonstrated that frequency-specific stimulation could provide informative and robust signals for learning. Taken together, these findings not only reveal novel features of the computational circuits underlying vibrotactile sensation, but they might guide the development of improved biomimetic stimulus strategies to artificially activate specific nuclei along the ascending somatosensory pathway for sensory neural prostheses.

bioRxiv preprint doi: https://doi.org/10.1101/2023.10.13.562210; this version posted October 17, 2023. The copyright holder for this preprint (which was not certified by peer review) is the author/funder, who has granted bioRxiv a license to display the preprint in perpetuity. It is made available under a CC-BY-NC-ND 4.0 International license.

Introduction

Vibrations are a fundamental component of our tactile experience. We use our ability to sense vibrations in many daily situations, such as perceiving incoming phone calls or detecting an approaching vehicle. In mammals, high frequency vibrations (>100Hz) are transduced to electrical signals by Pacinian corpuscles (PC), which are innervated by primary sensory neurons whose soma are situated in the dorsal root ganglia (DRG). This information is relayed to second order neurons in the dorsal column nuclei (DCN, gracile and cuneate) of the medulla. DCN axons project to neurons of the ventral posterolateral nucleus of the thalamus (VPL), which in turn project to the primary somatosensory cortex (S1). The earliest electrophysiological recordings from the receptor end organs (*1, 2*) revealed that the receptor potentials, as well as the resulting action potentials in DRG neurons, reliably time-lock to the cycles of a vibration up to 1000 Hz. However, little is known about how this precise temporal coding is processed in the rest of the central nervous system to achieve feature specific computation, commonly with a rate code.

In the medulla, only very few studies in cats have recorded neuronal responses to vibration, and they reported mostly 1:1 locking of spikes to the phase of the stimulus in low frequencies (*3–5*). In contrast, the VPL has been more extensively studied and is classically considered as a “relay nucleus” of the lemniscal pathway. Individual neurons were found to be occasionally temporally entrained, and there was an increasing complexity in preferred frequencies and neural adaptation to the vibration in this area (*6, 7*).

Finally, at the cortical level different coding modes have been described. On the one hand, in primate S1, vibration information seems to be represented by precise spiking patterns (*8, 9*), similar to the cutaneous mechanoreceptive afferents (*10, 11*). It is not until the secondary somatosensory cortex (S2), that the frequency-dependent firing rate modulations become the primary neural code for vibration and phase-locked responses seem absent (*12*). On the other hand, in rodent S1, neurons seem to represent vibration frequency by a rate code tuned to a preferred stimulus feature (*13*). This resembles the feature-selective coding found in many other sensory modalities (*13*). Yet it raises an important question: how are cyclically entrained action potentials (a temporal code) in afferents of peripheral mechanoreceptors transformed along the ascending neuraxis into a rate code in the cortex? In the current study, we addressed this question in mice by recording along the dorsal column medial lemniscus pathway to first uncover the basic coding principles and rules underlying sensory perception. Then, we sought to uncover the circuit mechanism underlying the transformation of neural coding with optogenetic manipulations. Finally, we tested to what extent these coding strategies might be leveraged as artificial sensory feedback in neuroprosthetics using microstimulation to selected neuronal populations. Overall, our results provide key insights into how to artificially mimic vibrotactile cues in neuroprosthetic devices.

Temporal code of vibrotactile stimuli along the ascending pathway

To identify the location and mechanism of the transformation of neural coding for vibration, we first conducted *in vivo* extracellular recordings in anesthetized mice along the ascending somatosensory pathway (**Fig. 1a**). Pure sinusoidal vibrations of a wide range of frequencies (100 Hz to 1900 Hz) (*13*) were delivered to the hindlimb of

bioRxiv preprint doi: https://doi.org/10.1101/2023.10.13.562210; this version posted October 17, 2023. The copyright holder for this preprint (which was not certified by peer review) is the author/funder, who has granted bioRxiv a license to display the preprint in perpetuity. It is made available under a CC-BY-NC-ND 4.0 International license.

anesthetized mice. We computed standardized inter-spike intervals (ISIs; see **Methods**) whose distribution should peak at integer multiples of the stimulus period in the case of phase-locked entrainment of action potentials by the oscillatory stimulus (**Fig. 1b-e** and **fig. S1**). Nerve recordings from low-threshold mechanoreceptors that are likely innervating Pacinian corpuscles (Aβ RA2-LTMR; **fig. S2**), display phase-locked spiking for vibrations up to 1900 Hz (**Fig. 1b**). We revealed that the precise temporal code found in the periphery is surprisingly well preserved in putative second-order neurons in the brainstem gracile nucleus (**Fig. 1c**). This reliable high-frequency spiking transmission in DCN likely relies on specialized mechanisms, possibly endocytic processes and synaptic structures (*14*). We therefore conducted reconstruction of focused ion beam scanning electron microscopy data of DCN synapses and expected to find structures similar to either the ribbon synapses in cochlear hair cells (*15*), or the calyx of Held in the auditory brainstem (*16*). However, we did not find evidence of either, suggesting that different mechanisms might govern high-throughput transmission in DCN (**fig. S3**).

In contrast to the reliable transmission revealed at the level of the DCN, the precise temporal code is lost in the ventral posterolateral nucleus of the thalamus (**Fig. 1d**) and remains absent in the somatosensory cortex (**Fig. 1e**). Phase-locking probability thus suddenly drops downstream of the brainstem (**Fig. 1f**), suggesting that the loss of temporal coding for vibration in the ascending pathway occurs at the level of the thalamus.

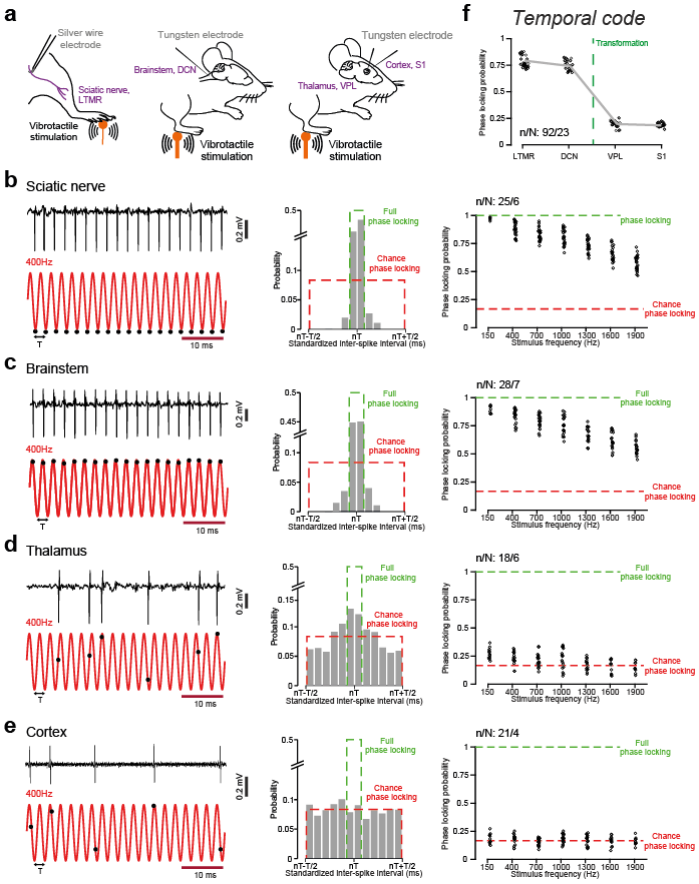


Fig. 1. Loss of temporal code for vibration beyond the brainstem in the ascending pathway. a, *In vivo* experimental setup schematic in anesthetized animals. Left, nerve fiber recording of sciatic nerve. Middle, recording of brainstem from the back of the neck. Right, recording of thalamus and cortex. **b,** Left, representative trace of a mechanosensitive afferent spiking in response to 400 Hz vibration stimulus. The timing of its action potentials (black dots) relative to periodic cycles of the vibration (red) shows nearly perfect entrainment. Middle, distribution of standardized inter-spike intervals of an example neuron at this frequency. Right, phase-locking probability measured for N = 25 neurons (6 mice) at each tested frequency (black circles). **c-e,** Similar logic as in **b**, for brainstem, thalamus and cortex, respectively. **f,** The phase-locking probability

bioRxiv preprint doi: https://doi.org/10.1101/2023.10.13.562210; this version posted October 17, 2023. The copyright holder for this preprint (which was not certified by peer review) is the author/funder, who has granted bioRxiv a license to display the preprint in perpetuity. It is made available under a CC-BY-NC-ND 4.0 International license.

compared between all four areas in the ascending pathway by averaging the results tested from 100 to 1900 Hz

Rate code of vibrotactile stimuli in the ascending pathway

The absence of cyclically phase-locked spiking beyond the brainstem suggests that vibration frequencies are represented as pure rate codes in both thalamus and cortex (*13*). However, the rate code for different vibration frequencies could also exist at the very early stages of the ascending pathway. We therefore investigated the feature-selective encoding of substrate vibrations within the same data as in **Figure 1**. Most of the vibration responsive units, even from nerve fibers, showed a frequency preference across various amplitudes (**Fig. 2a** and **fig. S4**). Nerve recordings revealed broad tuning curves covering a wide range of preferred frequencies (**Fig. 2b**), which indicated a moderate level of rate coding for vibration in the periphery. The pattern and distribution of tuning curves in the brainstem gracile nucleus were similar to the periphery (**Fig. 2c**). In contrast, the tuning curves in the ventral posterolateral nucleus of the thalamus became much more narrowly tuned (**Fig. 2d**), as did those in the somatosensory cortex (**Fig. 2e**). The comparison of the width of the tuning curves for vibration frequency from the periphery to the cortex (**Fig. 2f**), suggests that the main step causing a narrowing of the tuning found in S1 involves thalamic circuits. All together, our results show that the neural code transformation, from mechanoreceptor temporal encoding to the cortical rate encoding, thus mainly happens in thalamus (**Fig. 2g**).

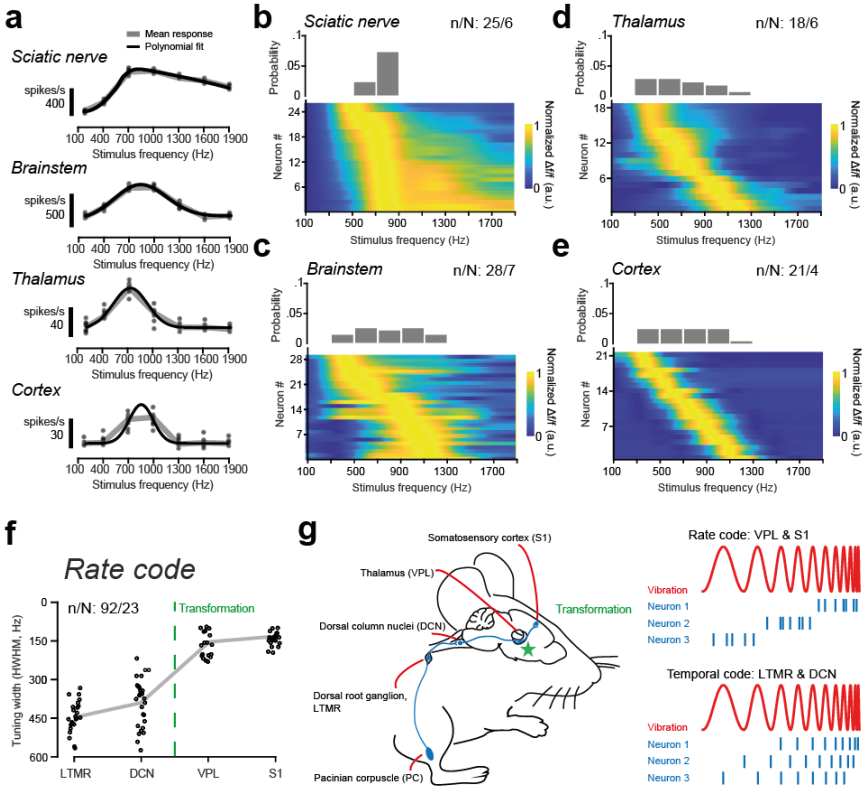


Fig. 2. Evolution of rate code for vibration of the ascending pathway. a, Tuning curves based on mean spike rates for example units recorded from peripheral nerve, brainstem, thalamus and cortex, respectively. **b,** Normalized tuning curves of all units from sciatic nerve recording with identifiable tuning curve peaks sorted by decreasing best frequency and distribution of neurons' best frequencies tested at 5 µm amplitude. **c-e,** Similar as in **b**, for brainstem, thalamus and cortex, respectively. **f,** The tuning curve, half-width at

bioRxiv preprint doi: https://doi.org/10.1101/2023.10.13.562210; this version posted October 17, 2023. The copyright holder for this preprint (which was not certified by peer review) is the author/funder, who has granted bioRxiv a license to display the preprint in perpetuity. It is made available under a CC-BY-NC-ND 4.0 International license.

the half-maximum of the curve (HWHM), for vibration frequency compared between all four areas in the ascending pathway (Kruskal–Wallis test, $P < 0.0001$). Dunn's Test: (S1=VPL)>(LTMR=DCN). **g,** A model for transformation of neural codes in the hindlimb dorsal column–medial lemniscal pathway.

The role of inhibitory thalamic circuits

According to previous work, the loss of the temporal code can be partially attributed to the strong, frequency-dependent depressing-type excitatory connections, which supply 'driver' type inputs (*17*) between DCN and VPL (*18*). However, this would not explain the significant narrowing of the rate code (**Fig. 2**). This aspect might be better explained by local interconnected feedforward and feedback circuits (*19–22*). To disentangle how the neural circuits within the thalamus could contribute to the transformation of the neural coding, we manipulated the neuronal activity with optogenetic tools. It has been shown that parvalbumin positive inhibitory interneurons participate in improving feature selectivity in the visual cortex (*23*) and controlling temporal firing patterns in spinal dorsal horn (*24*). In rodents, the sensory thalamus receives inhibitory drive from the thalamic reticular nucleus (*25, 26*). Here, we paired *in vivo* optogenetic stimulation through fiber optics with extracellular recordings in thalamic nuclei (**Fig. 3** and **fig. S5**).

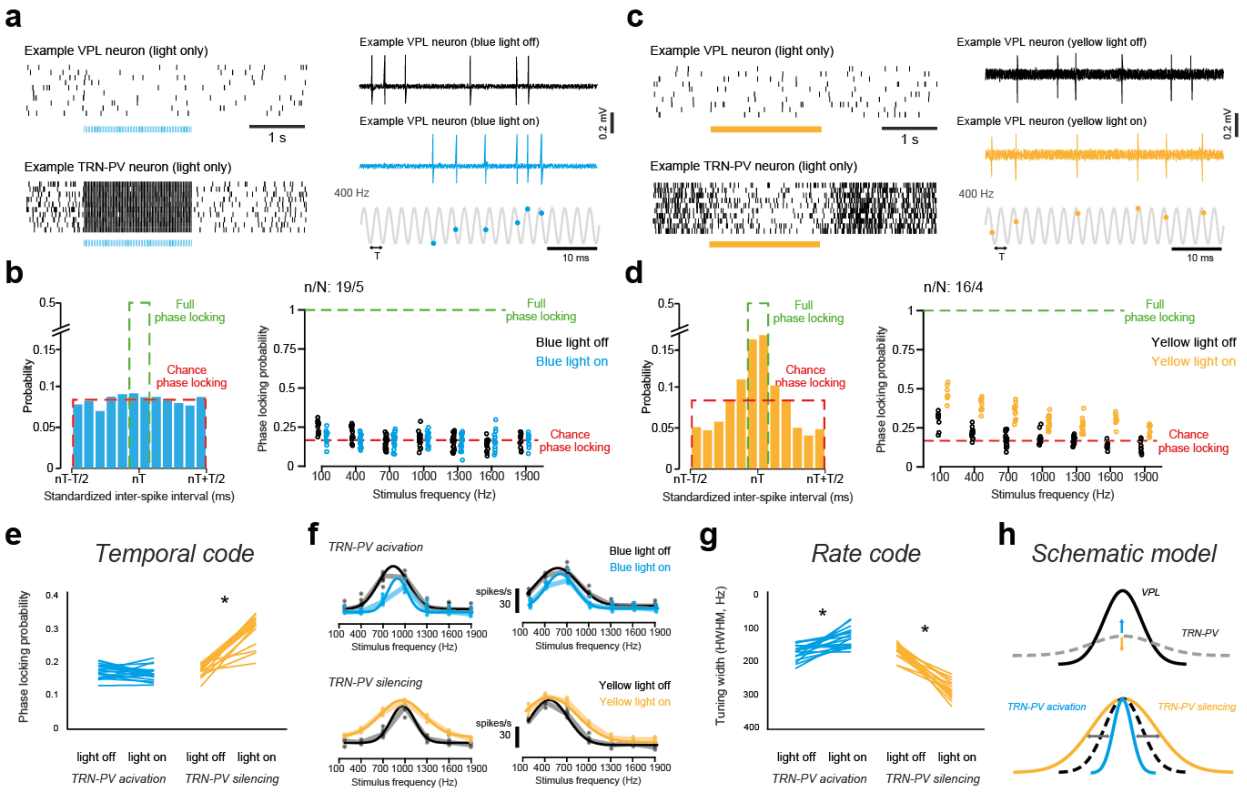


Fig. 3. Bi-directional optogenetic manipulation of parvalbumin neurons in thalamic reticular nucleus (TRN-PV) reveals its contribution to neural coding. a, Example recording of a VPL neuron (left top) and a TRN-PV neuron (left bottom) in response to 40 Hz (1ms pulses) of 473 nm blue light stimulation at TRN, in *PV-Cre* × *ChR2*-EYFP (Ai32)

bioRxiv preprint doi: https://doi.org/10.1101/2023.10.13.562210; this version posted October 17, 2023. The copyright holder for this preprint (which was not certified by peer review) is the author/funder, who has granted bioRxiv a license to display the preprint in perpetuity. It is made available under a CC-BY-NC-ND 4.0 International license.

mice. Right, example recording of a VPL neuron in response to 400 Hz vibration at the hindlimb, with light off (black) or with light on (blue). The timing of its action potentials (blue dots) relative to periodic cycles of the 400-Hz vibration (red) shows no sign of entrainment. **b,** Left, with blue light stimulation, the distribution of standardized inter-spike intervals of an example VPL neuron at 400 Hz vibration is nearly at random entrainment. Right, phase locking probability measured for n = 16 VPL neurons (6 mice) at each tested frequency evoking significant responses, either with light off (black circles) or with light on (blue circles). **c,** Example recording of a VPL neuron (left top) and a TRN-PV neuron (left bottom) in response to 2s continuous 568 nm yellow light stimulation at TRN, in *PV-Cre* × *ArchT*-GFP (Ai40) mice. Right, example recording of a VPL neuron in response to 400 Hz vibration at the hindlimb, with light off (black) or with light on (yellow). The timing of its action potentials (yellow dots) relative to periodic cycles of the 400-Hz vibration (red) shows little entrainment. **d,** Left, with yellow light stimulation, the distribution of standardized inter-spike intervals of an example VPL neuron at 400 Hz vibration is slightly above the chance entrainment. Right, phase locking probability measured for n = 17 VPL neurons (6 mice) at each tested frequency, for either with light off (black circles) or with light on (yellow circles). **e,** The phase-locking probability of VPL neurons affected by the optogenetic activation or inactivation of TRN-PV neurons (paired-sample t-test, *P < 0.0001). **f,** Top, tuning curve sharpening of 2 VPL example neurons after TRN-PV activation by blue light. Bottom, tuning curve broadening of 2 VPL example neurons after TRN-PV inactivation by yellow light. **g,** The frequency tuning width of VPL neurons affected by the optogenetic activation or inactivation of TRN-PV neurons (paired-sample t-test, *P < 0.0001). **h,** The schematic model showing how TRN-PV neurons sharpen the tuning curve of VPL neurons.

To achieve bi-directional optogenetic manipulation of parvalbumin neurons in the thalamic reticular nucleus (TRN-PV), we selectively expressed both excitatory Channelrhodopsin-2 (ChR2) and inhibitory Archaerhodopsin-3 (ArchT) in TRN-PV by using a double-transgenic strategy (*PV-Cre* × *ChR2*-EYFP, *PV-Cre* × *ArchT*-GFP, **fig. S5**). We first recorded TRN-PV and VPL neuron responses to blue light stimulation and to vibration stimuli paired with this optogenetic activation (**Fig. 3a**). We found that optogenetic activation of TRN-PV neurons did not alter the temporal processing for vibration in VPL (**Fig. 3b**). However, when we applied yellow light stimulation to inactivate the TRN-PV neurons in *PV-Cre* × *ArchT*-GFP mice (**Fig. 3c**), we found an improvement in the phase-locking probability of VPL neurons (**Fig. 3d**). Furthermore, we demonstrated that TRN-PV neurons are generally broadly tuned to vibration, and their inactivation can broaden the tuning width of VPL neurons (**Fig. 3g**, and **fig. S5**). We deduce that TRN-PV neuronal activity sharpens the frequency selectivity of VPL neurons and contributes to the loss of temporal coding (**Fig. 3e, f**). The mechanism by which they achieve this is thus similar to the broad inhibition that sharpens feature selectivity in the visual cortex (*23, 27*) (**Fig. 3h**).

Probing the neural coding mechanisms with microstimulation

To explicitly test if the coding mechanism described above could be used to artificially drive neurons in the somatosensory system (*28*), we probed the response of frequency selective neurons in S1 during temporally structured microstimulation applied to the DCN

bioRxiv preprint doi: https://doi.org/10.1101/2023.10.13.562210; this version posted October 17, 2023. The copyright holder for this preprint (which was not certified by peer review) is the author/funder, who has granted bioRxiv a license to display the preprint in perpetuity. It is made available under a CC-BY-NC-ND 4.0 International license.

and VPL (**Fig. 4a and fig. S6**) (*29*). First, the vibration frequency tuning of S1 neurons was determined using two photon calcium imaging in anesthetized *CaMKII-tTA* × *TRE*-GCaMP6s mice (see **Methods**). Subsequently, we characterized the response of the same S1 neurons to electrical stimulation (bipolar platinum–iridium electrodes) using matched frequencies of electrical pulses applied to the DCN (**Fig. 4b**). Microstimulation resulted in frequency selective tuning curves comparable to the tuning curves evoked by hindlimb vibration (**Fig. 4c**). To compare the responses of both modalities we calculated two indices: a "temporal coding index" (TCI, correlation of frequency tuning curves for vibration and electrical stimulation) and "rate coding index" (RCI, correlation of tuning curves to frequency invariant responses depending only on the number of pulses, see **Methods**). Equivalent experiments were then conducted with VPL stimulation (**Fig. 4d-e**). TCI and RCI show that the neural coding within DCN and VPL can be fully distinguished as a non-overlapping distribution (**Fig. 4f**). To further support this idea, the results from microstimulation within the spinal dorsal column paired with frequency selectivity readout at DCN also showed that the feedforward innervation from the periphery is mostly based on a temporal code (**fig. S7**). In conclusion, temporally precise microstimulation within the DCN, but not within the VPL, can reproduce S1 frequency tuning for vibration, confirming the significant differences in the neural coding mechanisms in these two areas (**Fig. 4g**).

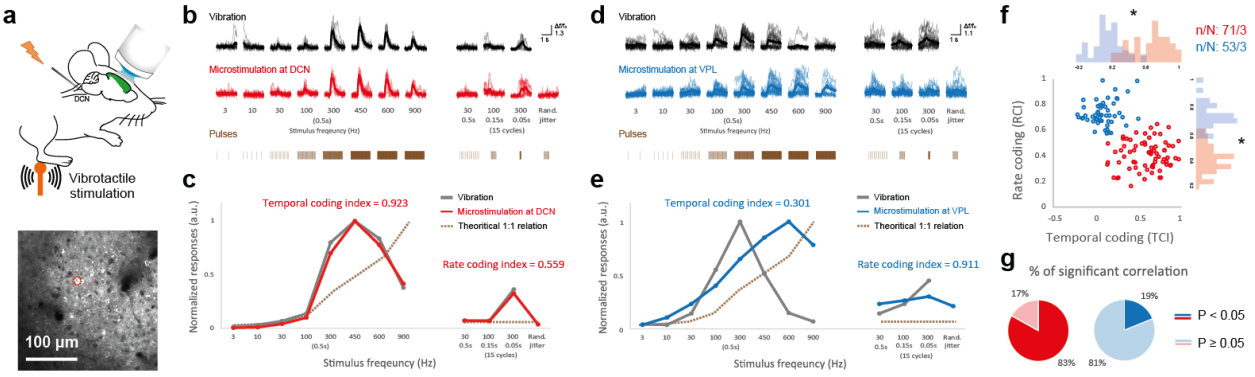


Fig. 4. Microstimulation reveals different neural codes for vibration in the brainstem and the thalamus. a, Experimental setup for two-photon calcium imaging in somatosensory cortex with CaMKII-tTA × TRE-GCaMP6s mice (top) and an example field-of-view (bottom). **b,** Top, averaged relative changes in fluorescence (Δf/f0) of an example S1 neuron imaged with two-photon microscopy in response to vibrations of different frequencies and durations. Bottom, averaged Δf/f0 of the same neuron imaged with two-photon microscopy in response to contralateral DCN microstimulation of different frequencies and durations. Background lines are responses to individual trials. **c,** Vibration frequency-selective tuning curve (gray) and DCN microstimulation frequency-selective tuning curves (red) of the example neuron in **b**. Gray dashed line, hypothetical response pattern predicted from the number of electrical pulses, assuming that the neuron increases its firing rate in a linear manner. Temporal coding index (TCI) and rate coding index (RCI) were computed from the tuning curves (see Methods). **d,** Top, averaged Δf/f0 of an example S1 neuron imaged with two-photon microscopy in response to vibrations of different frequencies and durations. Bottom, averaged Δf/f0 of the same

bioRxiv preprint doi: https://doi.org/10.1101/2023.10.13.562210; this version posted October 17, 2023. The copyright holder for this preprint (which was not certified by peer review) is the author/funder, who has granted bioRxiv a license to display the preprint in perpetuity. It is made available under a CC-BY-NC-ND 4.0 International license.

neuron imaged with two-photon microscopy in response to ipsilateral VPL microstimulation of different frequencies and durations. Gray lines are responses to individual trials. **e,** Vibration frequency-selective tuning curve (gray) and VPL microstimulation frequency-selective tuning curves (blue) of the example neuron in **d**. gray dashed line, hypothetical response pattern predicted from the number of the electrical pulse. **f,** The distribution of temporal coding index (TCI) and rate coding index (RCI) in both DCN (red) and VPL (blue) showed a very different coding strategies (paired-sample t-test, *P < 0.0001). **g,** The percentage of the S1 neurons whose vibration tuning curve can be reproduced by microstimulation tuning curves (Pearson's correlation).

Perceptual relevance of temporal code in the brainstem

Finally, we tested if DCN stimulation with high temporal precision could be perceived and thus potentially used for biomimetic feedback in neuroprosthetic devices. Because of the dense passage of fibers and the close proximity of nuclei involved in vital functions such interventions have not yet been attempted. We therefore developed a new chronic stimulation method that allows us to target the DCN unilaterally (see **Methods**). Inspired by other cortical microstimulation tasks (*30, 31*) we trained mice to perform a frequency discrimination task from artificial sensory stimulation (Fig. 5a, see **Methods**). Mice learned to discriminate 50 Hz from 300 Hz stimuli applied to the DCN (**Fig. 5b**) and S1 (**fig. S8**) and were then challenged to discriminate 50 Hz and 300 Hz from a 100 Hz standard on test days (**Fig. 5c**). This meant that 100 Hz was rewarded by right licks when compared to 50 Hz, but left licks when compared to 300 Hz, yet mice were able to generalize the rule of licking left for the lower frequencies and right for the higher frequencies. Overall, performance was better for 300 Hz (3/4 mice d' >1) than for 50 Hz (1/4 mice d' >1), compared to the 100 Hz standard. Most of the electrodes continued functioning even after two months of implantation (**fig. S9**). These results establish for the first time that mice can be chronically implanted with DCN electrodes by which frequency-specific stimulation can provide informative and robust signals for learning, comparable to, if not better than, classical cortical microstimulation in S1 (**fig. S8**).

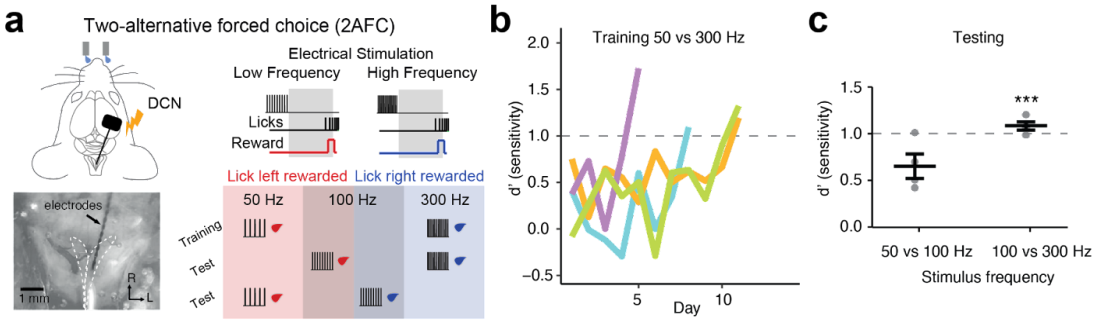


Fig. 5. Perception of artificial sensory stimulation through microstimulation. a, Schematic showing the two-alternative forced choice task (top left). Dorsal view of dorsal column nuclei (DCN) during electrode implantation. White dashed lines indicate the boundaries of the left and right gracile nuclei (bottom left). Mice were trained to discriminate electrical stimulation frequency pairs applied to the DCN. Comparison frequencies were either 50 Hz or 300 Hz compared to a 100 Hz standard. Stimuli were

bioRxiv preprint doi: https://doi.org/10.1101/2023.10.13.562210; this version posted October 17, 2023. The copyright holder for this preprint (which was not certified by peer review) is the author/funder, who has granted bioRxiv a license to display the preprint in perpetuity. It is made available under a CC-BY-NC-ND 4.0 International license.

applied for 0.5 s followed by a 2-second response window (gray shading). During the response window, licks to the right port for higher frequencies or left port for lower frequencies were rewarded and classified as hits. Licks to the left port for higher frequencies and right port for lower frequencies were classified as a miss, followed by a timeout of 2-4 seconds. No licks during the response window were counted as a non-response miss followed by a 2-second timeout before a new trial began. Mice learned to discriminate 50 Hz and 300 Hz during training, and this was reduced to 50 Hz compared to 100 Hz and 100 Hz compared to 300 Hz during test days. **b,** Learning curves represented as d-prime (d') calculated from hits and misses from mice discriminating 50 Hz from 300 Hz electrical stimulation to the DCN, over training days. Testing commenced after mice reached d' > 1 (gray dashed line) over 100 consecutive trials. **c,** Mean d' values for 50 Hz and 300 Hz comparison stimuli compared to the 100 Hz standard from testing days. Testing d' values were significantly greater for 100 vs 300 Hz discrimination, compared to the baseline mean d' values over the first three training days ($p = 0.0006$, one-way ANOVA, Bonferroni adjusted pairwise *post-hoc*), but not for 50 vs 100 Hz ($p = 0.051$, one-way ANOVA, Bonferroni adjusted pairwise *post-hoc*). Error bars represent S.E.M. ***$p < 0.001$.

Discussion

In the current study, we identified a circuit mechanism for the emergence of feature-selective encoding from peripheral mechanoreceptors along the ascending neuraxis, with a main transformation step at the level of the thalamus. Traditionally, the somatosensory thalamus is viewed as a simple relay for sensory information from the periphery to the higher brain regions (*32, 33*). In this study, we show that thalamus contributes to the transformation of neural coding from a temporal to a rate code. The role of this inhibitory thalamic circuit is reminiscent of how cortical parvalbumin-positive interneurons improve the feature selectivity, or how corticothalamic feedback sharpens the spatial tuning in the mouse visual system (*23, 34*). However, we cannot exclude contributions from other mechanisms of synaptic transmission. Future experiments, including cell patch clamp recording in brain slices of multiple regions along the ascending neuraxis might need to be conducted to allow for a more detailed characterization of the underlying synaptic mechanisms (*18, 35, 36*).

Our findings also suggest that inhibitory circuits within thalamus play a role in improving vibration frequency selectivity. In rats, topographic and stimulus-specific direct cortical excitation, and indirect inhibition through TRN, can selectively enhance or reduce VPM neuron spatial response tuning (*19*), which is consistent with the early evidence of lateral inhibition in the rat thalamus (*21, 37*).

The precise temporal coding in the somatosensory brainstem, at both the cellular and population level, might provide a significant advantage for potential brain machine interfaces. The manipulation of temporal patterns of electrical pulses through microstimulation is readily achievable, and does not require the characterization of detailed response properties and the targeting of individual neurons (*29*). In addition, the previously reported place code in DCN, where somatotopy and tonotopy were jointly observed, could be advantageous for reliably targeting neurons encoding spatial and temporal features of somatosensory stimuli, analogous to the artificial cochlea (*38*).

bioRxiv preprint doi: https://doi.org/10.1101/2023.10.13.562210; this version posted October 17, 2023. The copyright holder for this preprint (which was not certified by peer review) is the author/funder, who has granted bioRxiv a license to display the preprint in perpetuity. It is made available under a CC-BY-NC-ND 4.0 International license.

The remaining challenge is to understand the perceptual relevance of rate coding of vibration in thalamus and cortex. To directly test the hypothesis that the activation within a frequency-tuned neuron directly links to the perception of its preferred frequency in the animal, this precise manipulation could be achieved by sensory mapping with two-photon calcium imaging combining targeted multiphoton holographic optogenetics (*39, 40*) or by using the selective expression of channelrhodopsins such as a dual-protein switch system Cal-Light in the neural population responding to targeted frequency (*41*). These experiments are technically still very challenging but might be necessary to unequivocally reveal the coding scheme.

Finally, we hope our findings will help to understand how feature selectivity emerges in sensory systems, as transformation of neural coding from temporal to rate codes is also common in auditory and visual systems (*42, 43*). Moreover, detailed knowledge of the neural coding could assist the development of better neuroprosthetics in the ascending somatosensory pathway, and highlight the brainstem as a novel target for microstimulation (*44, 45*).

bioRxiv preprint doi: https://doi.org/10.1101/2023.10.13.562210; this version posted October 17, 2023. The copyright holder for this preprint (which was not certified by peer review) is the author/funder, who has granted bioRxiv a license to display the preprint in perpetuity. It is made available under a CC-BY-NC-ND 4.0 International license.

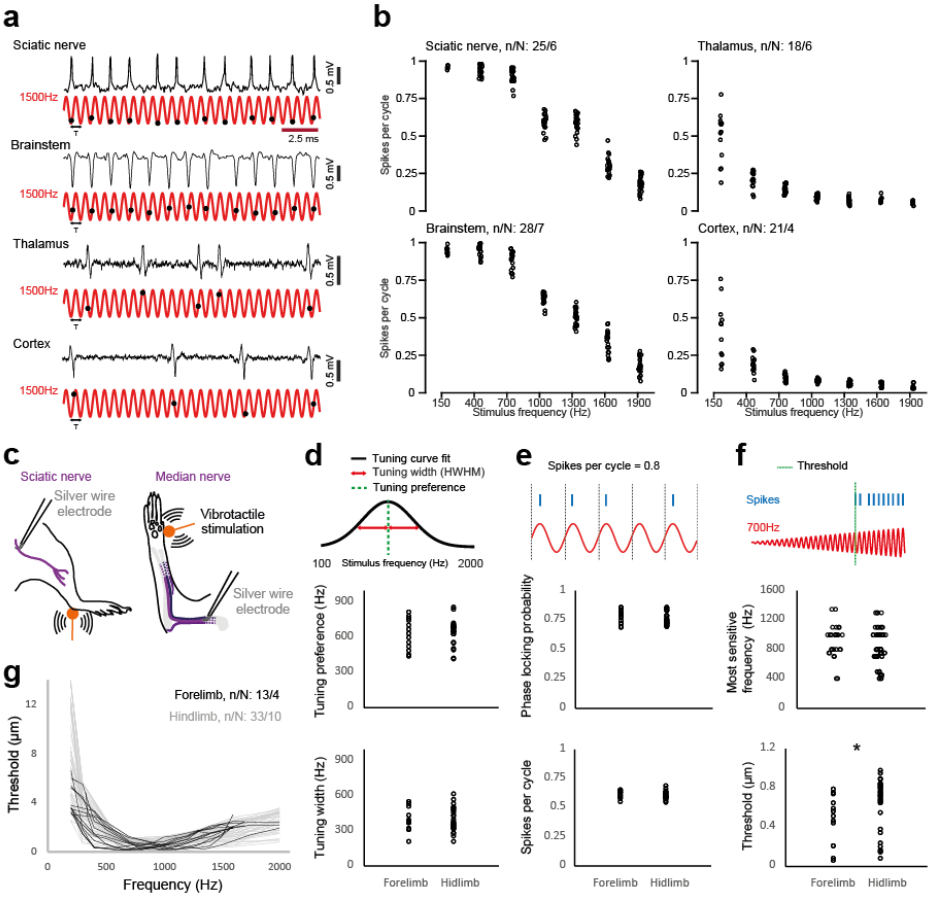


fig. S1. Responses properties to forelimb and hindlimb vibration in the ascending pathway.

a, Representative traces of four units spiking in response to 1500 Hz vibration stimulus. The timing of its action potentials (black dots) relative to periodic cycles of the vibration (red) shows different levels of phase-locking. **b,** Spiking probability within individual cycles of vibration measured at each tested frequency, for nerve, brainstem, thalamus and cortex, respectively. **c,** Experimental setup for nerve fiber recording of sciatic nerve and median nerve. **d,** The distribution of the tuning preference (top) and tuning width (bottom) measured from recording at hindlimb and forelimb. **e,** The distribution of the phase locking probability (top) and spiking probability (bottom) measured from both hindlimb and forelimb. **f,** The distribution of the most sensitive frequency (top) and threshold (bottom) measured at both hindlimb and forelimb (paired-sample t-test, *P = 0.027). **g,** Frequency dependent threshold curves (mechanical activation threshold versus stimulation frequency) for both hindlimb and forelimb.

bioRxiv preprint doi: https://doi.org/10.1101/2023.10.13.562210; this version posted October 17, 2023. The copyright holder for this preprint (which was not certified by peer review) is the author/funder, who has granted bioRxiv a license to display the preprint in perpetuity. It is made available under a CC-BY-NC-ND 4.0 International license.

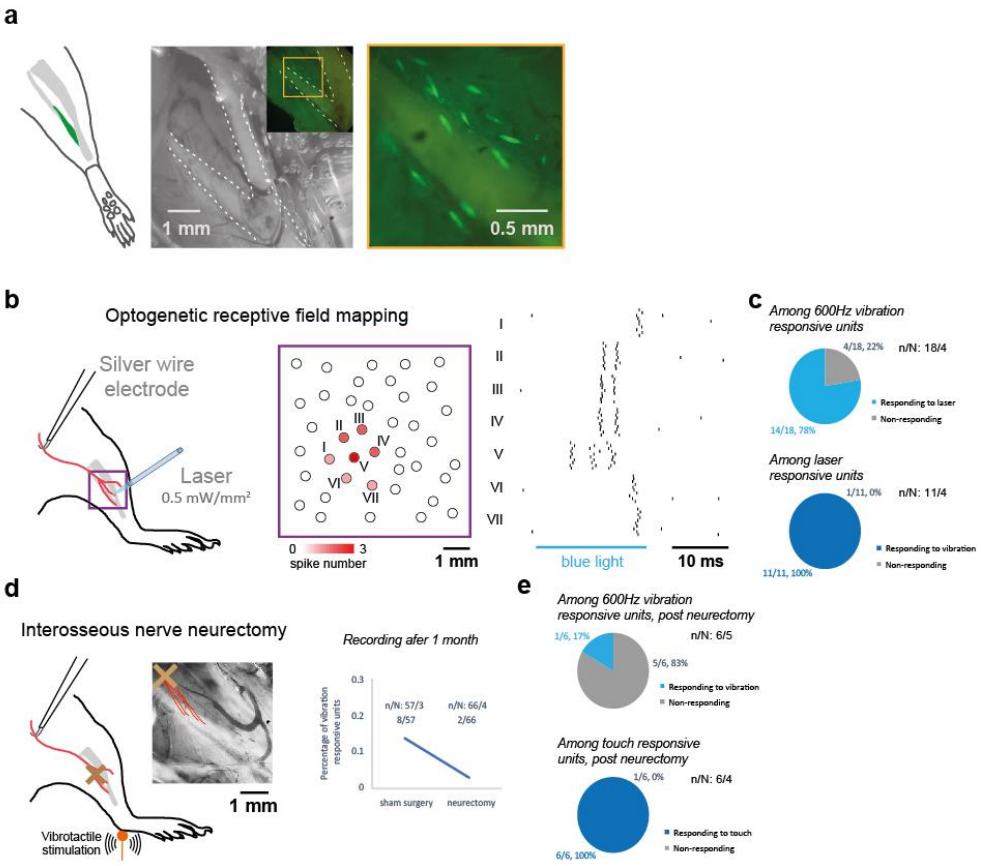


fig. S2. Identifying the origin of vibrotactile responses in hindlimb. a, Distribution of Pacinian corpuscles on the fibula in a mouse hindlimb, identified by EYFP expression in the inner core structures (green). **b,** Left, optogenetic stimulation on Pacinian corpuscles in *Etv1-Cre* × *ChR2*-EYFP (Ai32) mice. Middle. blue light pulses with 0.5-1 mm diameter were manually directed to the exposed fibula area at each location indicated by a circle, without presumption of the location of Pacinian corpuscles. Right, a Aβ RA-LTMR innervated by a Pacinian corpuscle expressing ChR2 in inner core cells responded with action potentials when the blue light was directed onto the location of the end organ. **c,** Top, out of 18 units that responded to 600 Hz vibration, 14 were activated by blue light illumination on the fibula. Bottom, all the laser responsive units are responding to vibration. **d,** Left, the schematic model of interosseous nerve neurectomy based on the nerve tracing. Right, after 1 month of neurectomy, terminal nerve recording showed the observation of vibration responsive units becoming very rare. **e,** During some terminal recording experiments, we directly compared the responsiveness of the same units pre- and post-neurectomy. Top, out of 6 units that responded to 600 Hz vibration, only 1 could still be activated by vibration post post-neurectomy. Bottom, all the touch responsive units were not affected by neurectomy.

bioRxiv preprint doi: https://doi.org/10.1101/2023.10.13.562210; this version posted October 17, 2023. The copyright holder for this preprint (which was not certified by peer review) is the author/funder, who has granted bioRxiv a license to display the preprint in perpetuity. It is made available under a CC-BY-NC-ND 4.0 International license.

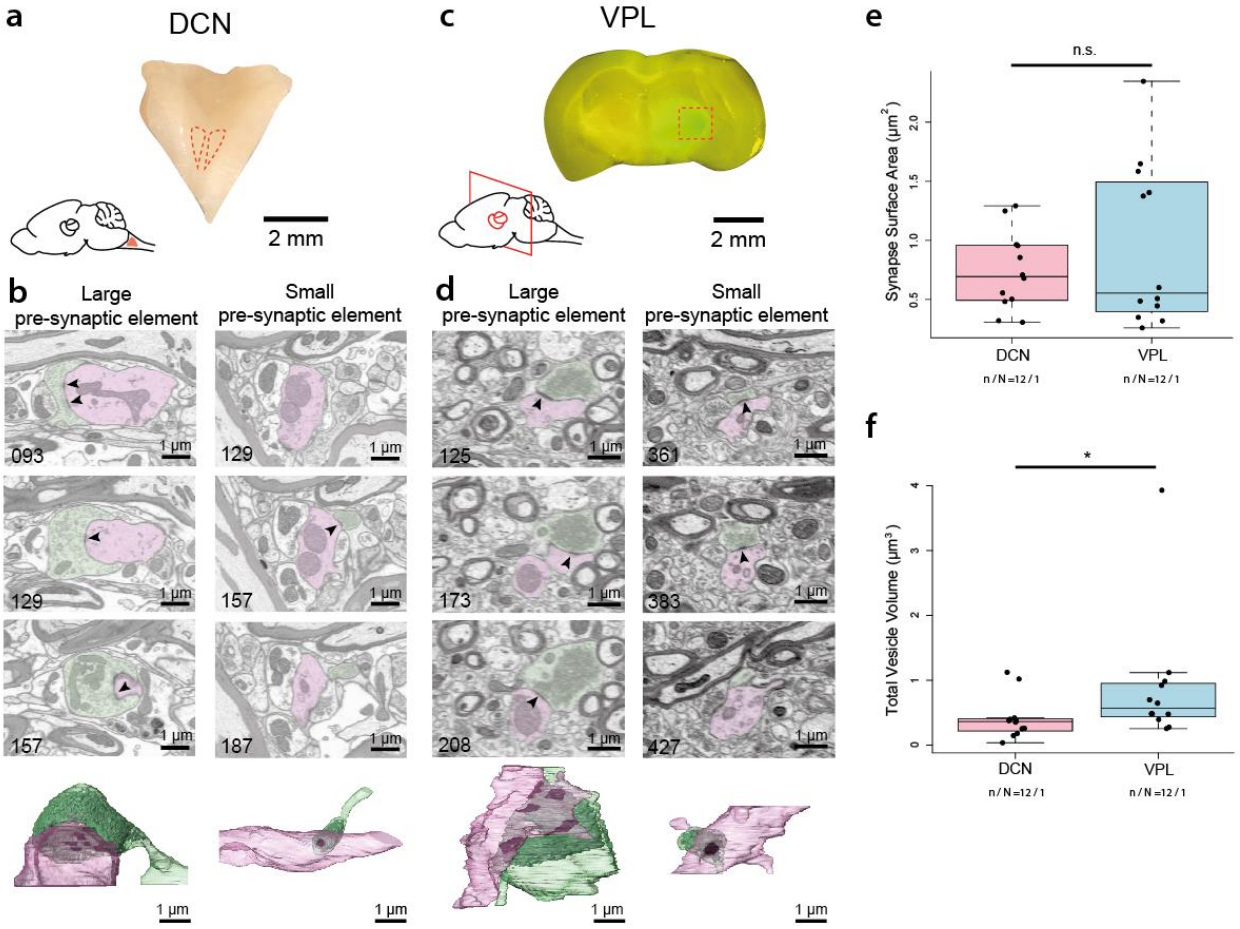


fig. S3. Electron microscopy analysis of synaptic structure of DCN and VPL. a, Dissected section of the brainstem. The dorsal column nuclei are indicated by the dotted red line. **b,** Two sample synapses in the DCN, one with a small and the other with a large presynaptic element. In the sample images from FIB-SEM, presynaptic elements are in green, postsynaptic elements are in pink and the arrowheads indicate synaptic electron-densities. In the respective reconstructions, presynaptic elements are in green, postsynaptic elements in pink, synapse in black and vesicles in gray. **c,** A GCaMP viral injection in hindlimb S1 retrogradely labels VPL projection neurons (green). This was used as a marker to identify VPL and dissect it for FIB-SEM. **d,** Same as **b** but the two sample synapses are from VPL. **e,** Distribution of total synaptic surface area per presynaptic element in DCN and VPL. Only synapses with large pre-synaptic elements (driver synapses) were included (n/N: 12/1, Wilcoxon rank-sum test, P = 0.7950). **f,** Distribution of total vesicle volume per presynaptic element in DCN and VPL (n/N: 12/1, Wilcoxon rank-sum test, P = 0.0304). Only synapses with large pre-synaptic elements (driver synapses) were included.

bioRxiv preprint doi: https://doi.org/10.1101/2023.10.13.562210; this version posted October 17, 2023. The copyright holder for this preprint (which was not certified by peer review) is the author/funder, who has granted bioRxiv a license to display the preprint in perpetuity. It is made available under a CC-BY-NC-ND 4.0 International license.

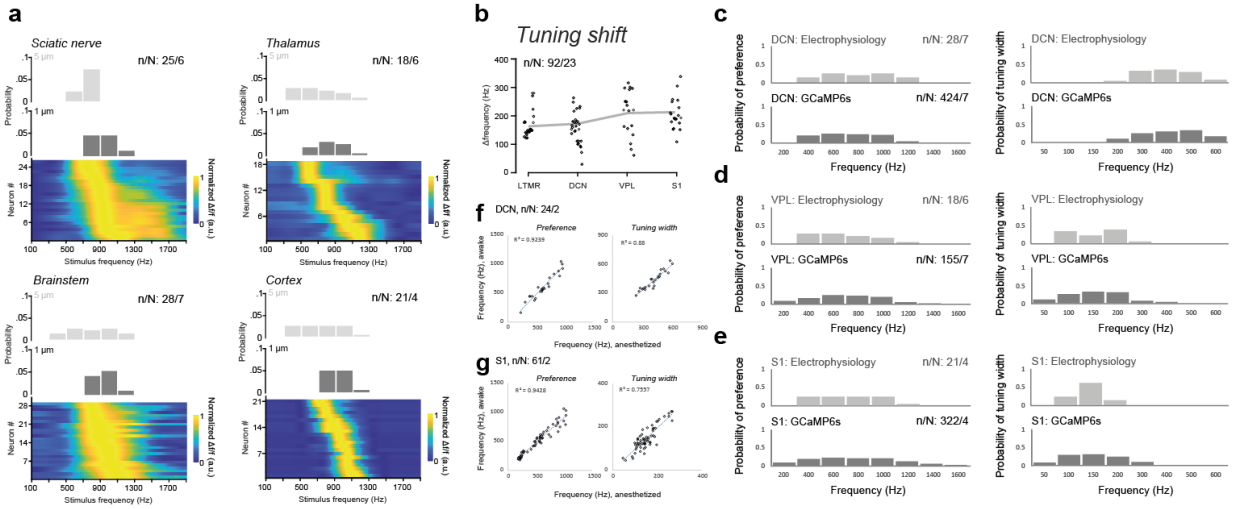


fig. S4. Frequency tuning depends on stimulus amplitudes, but not on recording methods. a, Normalized tuning curves of all neurons with identifiable tuning curve peaks sorted by decreasing best frequency and distribution of neurons' best frequencies tested at 5 µm (top) and 1 µm (middle and bottom) amplitude. **b,** The tuning shift for the preferred vibration frequency in different vibration amplitudes, compared between all four areas in the ascending pathway (Kruskal–Wallis test, P = 0.567). **c,** Left, the distribution of the tuning preference measured from the electrophysiology recording (top) or calcium imaging (bottom) at DCN. Right, the distribution of the tuning width measured from the electrophysiology recording (top) or calcium imaging (bottom) at DCN. **d,** Left, the distribution of the tuning preference measured from the electrophysiology recording (top) or calcium imaging (bottom) at VPL. Right, the distribution of the tuning width measured from the electrophysiology recording (top) or calcium imaging (bottom) at VPL. **e,** Left, the distribution of the tuning preference measured from the electrophysiology recording (top) or calcium imaging (bottom) at S1. Right, the distribution of the tuning width measured from the electrophysiology recording (top) or calcium imaging (bottom) at S1. No significant difference was found in any comparison between the results from electrophysiology and from imaging. **f,** Left, the correlation of the frequency preference of individual DCN neurons measured with calcium imaging either under anesthesia or awake condition. Right, the correlation of the tuning width of individual neurons (Pearson's correlation, P < 0.0001). **g,** Left, the correlation of the frequency preference of individual S1 neurons measured with calcium imaging either under anesthesia or awake condition. Right, the correlation of the tuning width of individual neurons (Pearson's correlation, P < 0.0001).

bioRxiv preprint doi: https://doi.org/10.1101/2023.10.13.562210; this version posted October 17, 2023. The copyright holder for this preprint (which was not certified by peer review) is the author/funder, who has granted bioRxiv a license to display the preprint in perpetuity. It is made available under a CC-BY-NC-ND 4.0 International license.

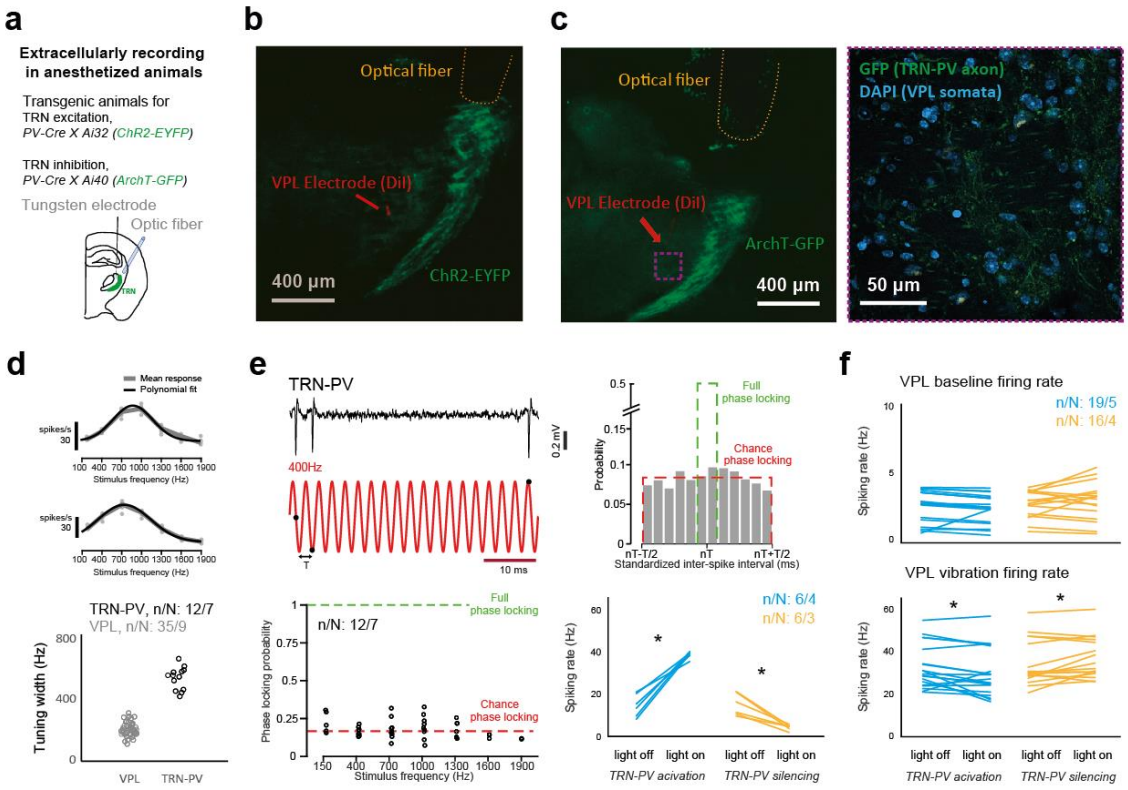


fig. S5. Response properties to vibration of TRN-PV neurons and effects of optogenetic stimulation on thalamic nuclei. a, Experimental setup for paired optogenetic stimulation and extracellular recordings in thalamic nuclei. **b,** Post hoc histology demonstrates the YFP expression of TRN-PV neurons in *PV-Cre* X Ai32 mice and the electrode/optical fiber implantation can be localized. **c,** Left, coronal brain slice shows the GFP expression of TRN-PV neurons in *PV-Cre* X Ai40 mice and the electrode/optical fiber implantation can be localized. Right, the GFP signal within VPL is only present in axons, not in somas. **d,** Top, tuning curves based on mean spike rates of two opto-tagged TRN neurons. Bottom, the distribution of tuning width of VPL and TRN-PV neurons (Wilcoxon rank-sum test, $P < 0.0001$). **e,** Top left, representative trace of a TRN-PV neuron spiking in response to 400 Hz vibration stimulus. The timing of its action potentials (black dots) is overlaid with periodic cycles of the vibration (red). Top left, distribution of standardized inter-spike intervals of an example neuron at this frequency. Bottom right, phase-locking probability measured at each tested frequency. Bottom right, the spiking rate of TRN-PV neurons affected by the optogenetic activation or inactivation (paired-sample t-test, $*P < 0.0001$). **f,** Top, the baseline spiking rate of VPL neurons affected by the optogenetic activation or inactivation of TRN-PV neurons. Bottom, the spiking rate during vibration stimulus of VPL neurons affected by the optogenetic activation or inactivation of TRN-PV neurons (paired-sample t-test, $*P < 0.0001$)

bioRxiv preprint doi: https://doi.org/10.1101/2023.10.13.562210; this version posted October 17, 2023. The copyright holder for this preprint (which was not certified by peer review) is the author/funder, who has granted bioRxiv a license to display the preprint in perpetuity. It is made available under a CC-BY-NC-ND 4.0 International license.

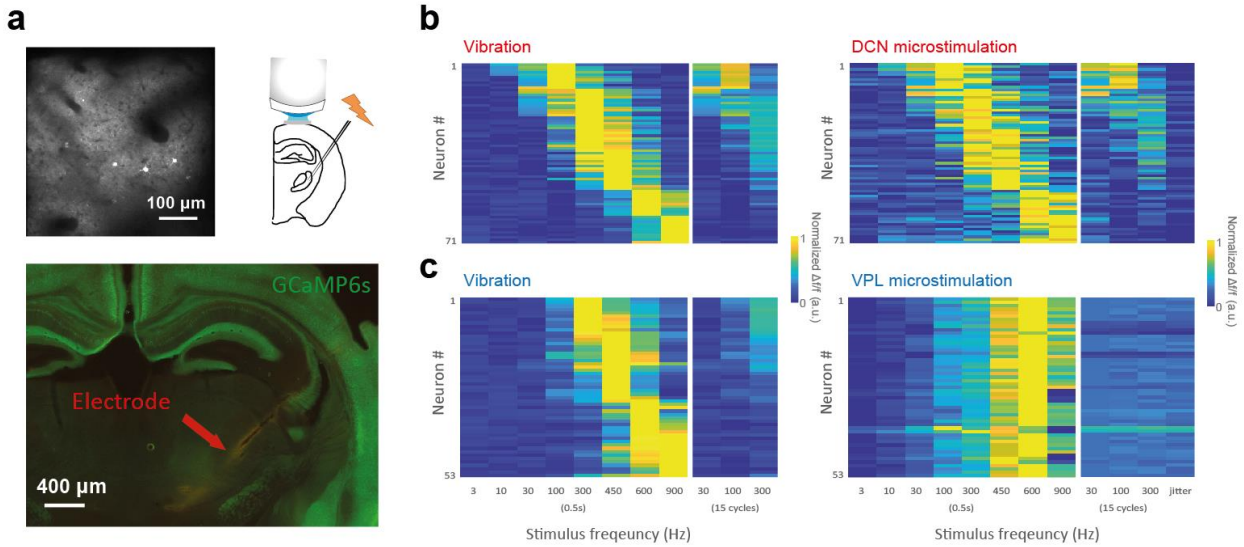


fig. S6. Microstimulation in DCN and VPL with readout in S1. a, Top, experimental setup for two-photon calcium imaging paid with electrical stimulation in VPL and an example field-of-view in S1. Bottom, an example tract of the electrode in histology. **b,** Left, frequency-selective tuning curves of S1 neurons in response to vibrations of different frequencies and durations. Right, frequency-selective tuning curves of the same S1 neurons in response to DCN microstimulation of different patterns and durations. **c,** Left, frequency-selective tuning curves of S1 neurons in response to vibrations of different frequencies and durations. Right, frequency-selective tuning curves of the same S1 neurons in response to VPL microstimulation of different patterns and durations.

bioRxiv preprint doi: https://doi.org/10.1101/2023.10.13.562210; this version posted October 17, 2023. The copyright holder for this preprint (which was not certified by peer review) is the author/funder, who has granted bioRxiv a license to display the preprint in perpetuity. It is made available under a CC-BY-NC-ND 4.0 International license.

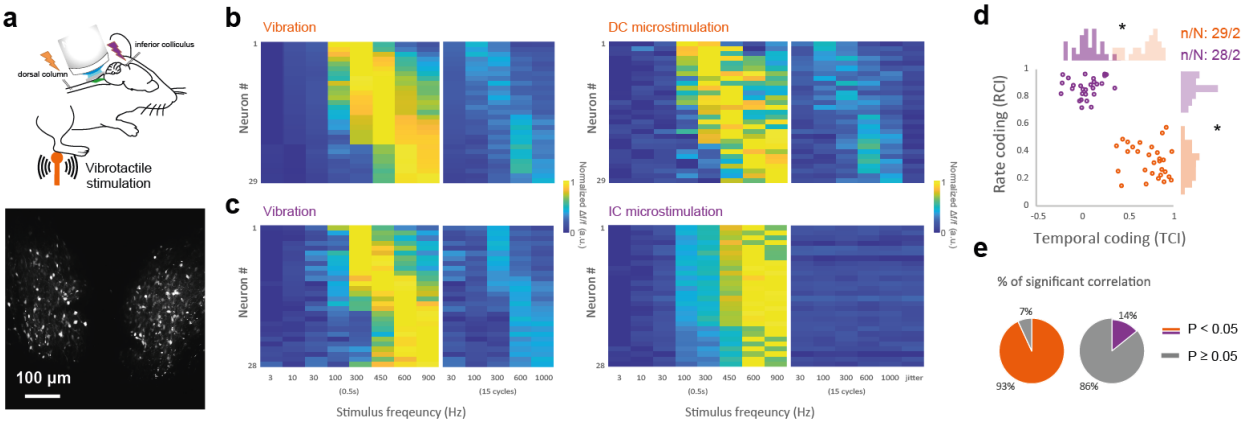


fig. S7. Microstimulation in dorsal horn of lumbar spinal cord and inferior colliculus with readout in DCN. a, Top, experimental setup for two-photon calcium imaging paid with electrical stimulation in the dorsal horn (DC) of lumbar spinal cord and inferior colliculus (IC), the unidirectional feedforward target of DCN. Bottom, an example field-of-view in DCN. **b,** Left, frequency-selective tuning curves of DCN neurons in response to vibrations of different frequencies and durations. Right, frequency-selective tuning curves of the same DCN neurons in response to DC microstimulation of different patterns and durations. **c,** Left, frequency-selective tuning curves of DCN neurons in response to vibrations of different frequencies and durations. Right, frequency-selective tuning curves of the same DCN neurons in response to IC microstimulation of different patterns and durations. **d,** The distribution of temporal coding index (TCI) and rate coding index (RCI) in both DC (orange) and IC (purple) showed a very different coding strategies (paired-sample t-test, *P < 0.0001). **e,** The percentage of the DCN neurons whose vibration tuning curve can be reproduced by microstimulation tuning curves (Pearson's correlation).

bioRxiv preprint doi: https://doi.org/10.1101/2023.10.13.562210; this version posted October 17, 2023. The copyright holder for this preprint (which was not certified by peer review) is the author/funder, who has granted bioRxiv a license to display the preprint in perpetuity. It is made available under a CC-BY-NC-ND 4.0 International license.

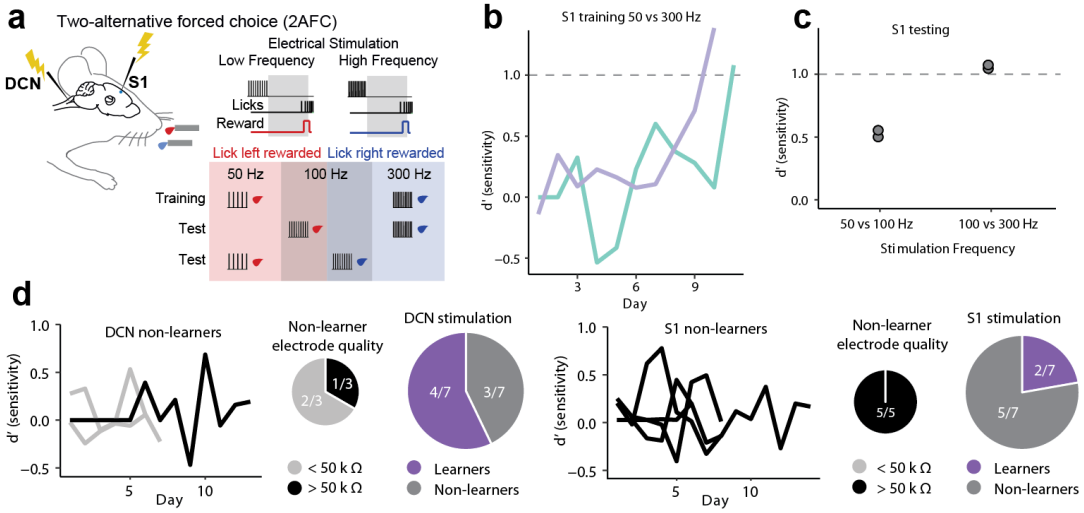


fig. S8. Perception of artificial sensory stimulation through microstimulation of S1. **a,** Schematic showing the two-alternative forced choice task. For a full description of the task, see **Fig. 5** legend. **b,** Learning curves represented as d' calculated from hits and misses from mice discriminating 50 Hz from 300 Hz electrical stimulation to S1, over training days. Testing commenced after mice reached d' > 1 (gray dashed line) over 100 consecutive trials. **c,** Mean d' values for 50 Hz and 300 Hz comparison stimuli compared to the 100 Hz standard from testing days. **d,** Learning curves, as in b for mice that failed to learn the task, for DCN stimulation (left) and S1 stimulation (right). Pie charts to the right of each panel show the proportions of mice that learned or did not learn the task. Two of the three DCN stimulation non-learners had electrodes that failed, whereas none of the S1 non-learners had failed electrodes.

bioRxiv preprint doi: https://doi.org/10.1101/2023.10.13.562210; this version posted October 17, 2023. The copyright holder for this preprint (which was not certified by peer review) is the author/funder, who has granted bioRxiv a license to display the preprint in perpetuity. It is made available under a CC-BY-NC-ND 4.0 International license.

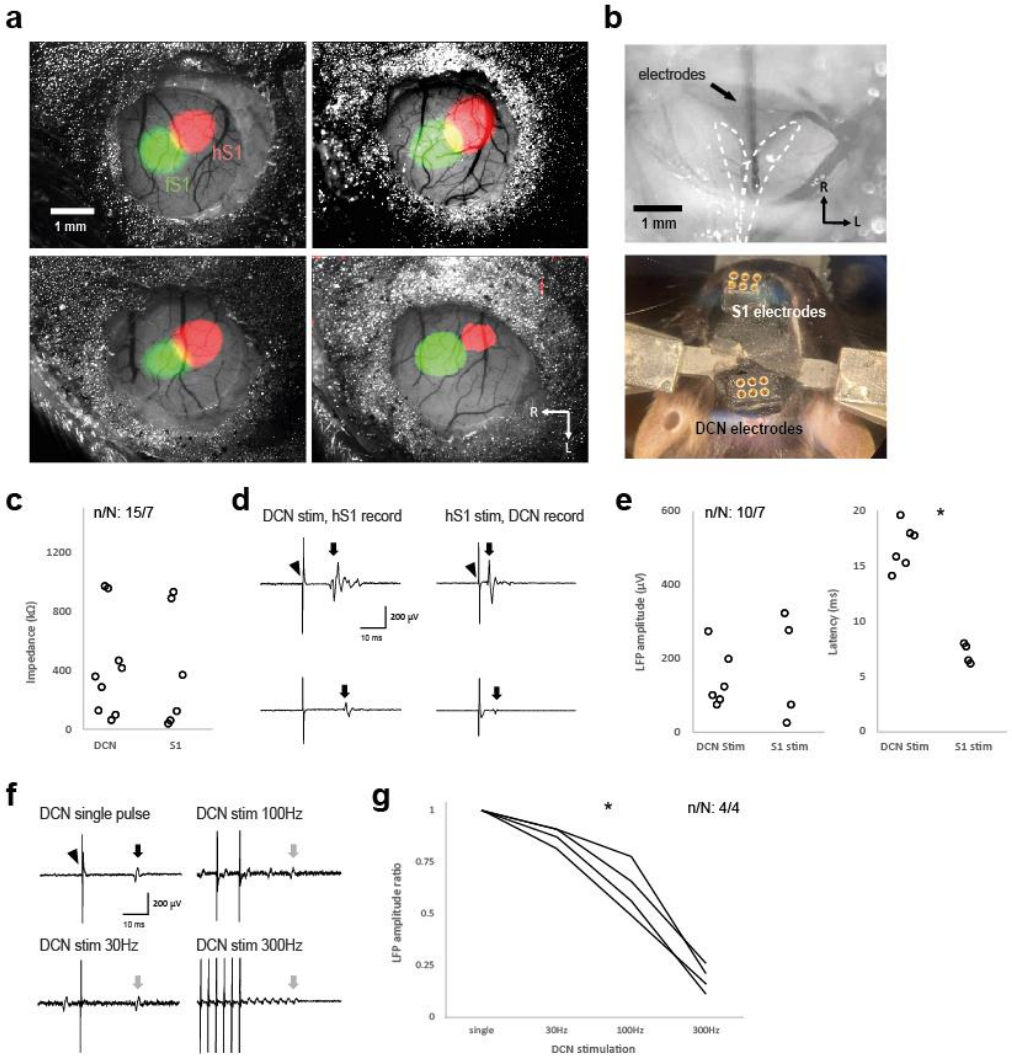


fig. S9. Validation of microstimulation with local field potential recording. a, An example of cranial windows and location for electrode implantation. The targeted area is determined based on the position of the hindlimb S1 (hS1, red) defined with intrinsic signal imaging, neighboring to the forelimb S1 (fS1, green). **b,** Top, dorsal view of dorsal column nuclei (DCN) during electrode implantation. White dashed lines indicate the boundaries of the left and right gracile nuclei. Bottom, 5 weeks after the surgery. **c,** The impedance of electrodes in DCN and S1 after at least 3 weeks of implantation. **d,** Left, two example DCN stimulus-evoked local field potential (LFP) responses in hS1 (arrow). Right, two example hS1 stimulus-evoked local field potential responses in DCN (arrow). Arrowhead indicates the stimulus artifact. **e,** Left, the LFP amplitudes across all recordings. Right, the latency of LFP across all recordings (Wilcoxon rank-sum test, $P < 0.0001$). **f,** Example DCN stimulus-evoked LFP in hS1 with different stimulation patterns. Gray arrows indicate the LFP responding to the last electrical pulse of a 0.5 second stimulation train. **g,** Normalized LFP amplitudes across different stimulation frequencies (one-way repeated measures ANOVA, $P < 0.0001$). All LFP traces were averaged across 100 trials.

bioRxiv preprint doi: https://doi.org/10.1101/2023.10.13.562210; this version posted October 17, 2023. The copyright holder for this preprint (which was not certified by peer review) is the author/funder, who has granted bioRxiv a license to display the preprint in perpetuity. It is made available under a CC-BY-NC-ND 4.0 International license.

Materials and Methods

Animals

Electrophysiology and imaging experiments at different parts of the ascending pathway were conducted with C57BL/6 (Charles River Laboratory) mice. Experiments involving optogenetic manipulation of thalamic inhibitory circuits were conducted in double-transgenic mice generated by mating homozygous Ai32 mice carrying a floxed *ChR2*-EYFP fusion gene inserted in the *Gt(ROSA)26Sor* locus in a C57BL/6 strain (Jackson Laboratory; stock no. 012569) or homozygous Ai40 mice carrying a floxed *ArchT*-EYFP fusion gene inserted in the *Gt(ROSA)26Sor* locus in a C57BL/6 strain (Jackson Laboratory; stock no. 021188) with homozygous *PV-Cre* (Jackson laboratory; stock no. 017320) mice. As such, Cre-mediated recombination resulted in an expression of the floxed opsin sequence in the PV-expressing cells of the offspring. Imaging experiments involving calcium imaging in S1 were conducted in double-transgenic *CaMKII*-GCaMP6s mice generated by mating heterozygous *CaMKII-tTA* mice (Jackson Laboratory; stock no. 007004) and *TRE*-GCaMP6s mice (Jackson Laboratory; stock no. 024742). CaMKII-GCaMP6s mice express the neural activity indicator GCaMP6s (*46*) in excitatory neurons of the cortex (*47*). Hindpaw optogenetic stimulation of Pacinian corpuscle were conducted in double-transgenic mice generated by mating homozygous Ai32 mice with heterozygous *ER81/Etv1*-CreER mice expressing the CreER^{T2} fusion protein from the ER81/Etv1 promoter elements (Jackson Laboratory; stock no. 013048). As such, Cre-mediated recombination resulted in an expression of the floxed ChR2 sequence in the *ER81/Etv1*-expressing cells of the offspring. ER81/Etv1 is expressed in the inner core region of Pacinian corpuscles. To induce CreER-based recombination, double-transgenic adult offspring were administered one daily dose of a 100 µL tamoxifen (T5648, Sigma-Aldrich) solution (20 mg/mL) dissolved in corn oil (C8267, Sigma-Aldrich) for five consecutive days by peritoneal injection. Wild type mice were purchased from Charles River and transgenic mice were obtained from The Jackson Laboratory and bred in the animal facility of the University of Geneva.

Mice were housed in an animal facility, maintained on a 12:12 light/dark cycle, and the experiments were performed during the light phase of the cycle. The animals did not undergo any previous surgery, drug administration or experiments and were housed in groups of maximum 5 animals per cage. All procedures complied with and were approved by the Institutional Animal Care and Use Committee of the University of Geneva and Geneva veterinary offices.

Surgery

15 to 30 week old mice were surgically prepared for terminal two-photon Ca^{2+} imaging. Surgeries were conducted under isoflurane anaesthesia (1.5 to 2%) and additional analgesic (0.1 mg/kg buprenorphine intramuscular (i.m.)), local anaesthetic (75 µL 1% lidocaine subcutaneous (s.c.) under the location for incision) and anti-inflammatory drugs (2.5 mg/kg dexamethasone i.m. and 5 mg/kg carprofen s.c.) were administered. Mice were fixed on a bite bar with a snout clamp and rested on top of a heating pad. For viral expression at the brainstem, thalamus and cortex, the scalp was cut over the midline between the ears and eyes. After removing the dura, a bulk viral injection (400 to 800 nL) was administered with pulled and bevelled glass pipettes (≈15 µm tip diameter) at an approximate rate of 20 nL/min into either, the gracile nucleus right next to the obex, the

bioRxiv preprint doi: https://doi.org/10.1101/2023.10.13.562210; this version posted October 17, 2023. The copyright holder for this preprint (which was not certified by peer review) is the author/funder, who has granted bioRxiv a license to display the preprint in perpetuity. It is made available under a CC-BY-NC-ND 4.0 International license.

ventral posterolateral nucleus (VPL), nucleus of the thalamus (2 mm lateral and 2 mm posterior to bregma; 3.5 mm below the dura), or the hindlimb representation of the primary somatosensory cortex (2 mm lateral and 0 mm to anterior to bregma; 350 µm below the dura). For a dense expression among the neural population, the injections consisted of AAV1.Syn.GCaMP6f.WPRE.SV40 (University of Pennsylvania, CS0939, titer 6.93 x 10^{13}), AAV1.Syn.GCaMP6s.WPRE.SV40 (University of Pennsylvania, CS0205, titer 3.22 x 10^{13}), or AAVrg.Syn.jGCaMP7b.WPRE (Addgene, lot. no. v63074, titer 1 x 10^{13}). For GCaMP expression in the DRG neurons, AAV5.CAG.GCaMP6s.WPRE.SV40 (Addgene, lot. no. v20751, titer 3.2 x x 10^{13}), or AAV1.CAG.GCaMP6s.WPRE.SV40 (University of Pennsylvania, V3096TI-3, titer 2.33 x 10^{13}) was directly injected (1000 to 3000 nL) into the lumbar enlargement in between T13 and L4 vertebrates. For visualizing the process of injection, 0.1 µL of 2% FastGreen was added into 5 µL of the virus. After the end of each injection, the pipette was left in place for at least another 10 min before being retracted. After 3-8 weeks of expression and recovery, experiments could be conducted.

All imaging and electrophysiology experiments were surgically prepared under terminal anesthesia by inhalation of isoflurane (~2%) and the body temperature was maintained near 37 °C. For analgesia, buprenorphine (0.1mg/kg SC) was provided 15-20 min before the procedure, except for thalamus and cortex, where chronic preparation was employed. An additional dose of buprenorphine was given if the procedure exceeded 4 hours. The whole procedure was limited to 8 hours. For imaging of brain structures, a custom-made titanium head bar was fixed on the skull with a cyanoacrylate adhesive (ergo 5011, IBZ Industrie) and dental cement to allow subsequent head fixation.

Imaging of dorsal root ganglia (DRG) was done at least four weeks after GCaMP expression. The surgical procedure for vertebral window implantation was adapted from a previous study (*48*). In short, after hemostasis, DRG was covered with a thin layer of Kwik-Sil silicone elastomer (World Precision Instruments) and sealed with a 2-mm diameter cover glass, and the cover glass was attached to the vertebral mount by cyanoacrylate glue and dental acrylic.

For brainstem imaging, the skin and cervical paraspinal muscle over the neck were cut and pulled to the side. A custom made titanium head bar was fixed on the skull with a cyanoacrylate adhesive (ergo 5011, IBZ Industrie) and dental cement. The head was fixed at approximately 45° downward. After the removal of dura and the skull above the posterior part of the cerebellum, Kwik-Sil was applied to the surface of the brainstem before a hand-cut wedge-shaped glass coverslip (150 µm thickness) was placed over the brainstem. The glass window over the gracile nucleus was first stabilized by the pressure of a micromanipulator. The micromanipulator was removed after the cyanoacrylate glue and dental acrylic hardened.

For thalamic and cortical imaging, survival surgery for window implantation was performed either right after viral injection or after 2-4 weeks of recovery period and viral expression. A craniotomy was performed over the target structures. For the cortical imaging, two hand-cut glass coverslips (150 µm thickness) matched to the shape of the craniotomy were glued together with optical adhesive (NOA 61, Norland Products). The lower glass was placed on top of the cortex, and the upper glass, which was larger than the craniotomy, was glued to the skull with cyanoacrylate adhesive and secured with dental cement. For the cortical imaging using transgenic mice, viral injections were skipped. For thalamic imaging, a gradient-index (GRIN) lens (Inscopix) was used instead of a glass coverslip. The correspondence between the injection sites and the sensory hindpaw representation was confirmed during *in vivo* sensory mapping.

bioRxiv preprint doi: https://doi.org/10.1101/2023.10.13.562210; this version posted October 17, 2023. The copyright holder for this preprint (which was not certified by peer review) is the author/funder, who has granted bioRxiv a license to display the preprint in perpetuity. It is made available under a CC-BY-NC-ND 4.0 International license.

Two-photon Ca^{2+} imaging

Imaging was performed with a custom-built two-photon microscope (MIMMS, www.openwiki.janelia.org) controlled by Scanimage 5.1 (Vidrio Technologies) using a 16X 0.8 NA objective (Nikon) and with excitation wavelength set to ~920 nm (Ultra II, tunable Ti:Sapphire laser, Coherent). 512 by 512 pixel images were acquired at 29.72 Hz using bidirectional scanning with a resonant scanner system (Thorlabs). The power was modulated with a Pockels cell (350-80-LA-02, Conoptics) and calibrated with a photodiode (Thorlabs). The primary mirror for imaging was a custom polychroic (Chroma, zt470/561/nir-trans) that could transmit infrared light, while reflecting green light. Before detection, the remaining infrared light was filtered with a coloured glass band pass filter (BG39, Chroma). Images were acquired using photomultiplier tubes (H11706P-40 SEL, Hamamatsu) and written in 16 bit format to disk.

Raw calcium images were processed using Suite2P, a publicly available two-photon calcium imaging analysis pipeline (*49*). First, images were registered based on the cross-correlation of the averaged images to account for brain motion. Then, regions of interest (ROI) were established by clustering neighboring pixels with similar time courses. Next, manual selection of ROI was performed to eliminate low-quality or non-targeted regions of interest.

Intrinsic signal imaging

Intrinsic signal imaging was performed to precisely localize the hindlimb representation of S1 for electrode implantation. Mice were head-fixed and placed on a heated platform under light isoflurane anesthesia (0.25 to 0.75%). Their right forepaw or hindpaw rested on a metal rod (2 mm diameter) mounted on a galvanometric actuator (model. no. 000-G120D, GSI Lumonics). Fifteen 1-s vibrotactile stimuli consisting of a 100 Hz sinusoidal vibration were delivered to the forepaw with a 10 s inter-stimulus interval. The cranial window was illuminated with a collimated red light LED (635 nm peak, ACULED VHL, part. no. E001947, Perkin Elmer) and imaged with a CCD camera at 10 fps with 256 × 332 pixel resolution (Retiga-2000R, Q Imaging). The average difference image between the stimulation period and a 1.5-s baseline period was processed using a 50 × 50-pixel spatial averaging filter and subsequently smoothed with a 5 × 5-pixel Gaussian lowpass filter with 0.5 pixel s.d. Stimulus presentation and image acquisition were controlled using Ephus software (https://Scanimage.org).

Electrophysiology

For electrophysiology experiments, the mice were anesthetized by isoflurane inhalation (2%) and body temperature was maintained near 37 °C with a heating mat. For analgesia, buprenorphine (0.1mg/kg SC) was provided 15-20 min before the procedure. To assess the sensory afferents innervating Pacinian corpuscles, a skin opening was performed along the hamstring muscle. Then, the sciatic nerve was carefully isolated using ophthalmic scissors and tweezers. The pia mater spinalis and dura mater around the nerve were removed, and finally, the nerve bundle was separated into single fibers (15-20 µm in diameter) and placed on two Ag/AgCl wire electrodes in the recording pool filled with mineral oil. A third ground Ag/AgCl electrode was placed in the muscle next to the recording chamber.

To characterize the response properties of sensory afferents at the peripheral level, we recorded stimulus-evoked activity of afferents *in vivo* using hook electrodes in the both

bioRxiv preprint doi: https://doi.org/10.1101/2023.10.13.562210; this version posted October 17, 2023. The copyright holder for this preprint (which was not certified by peer review) is the author/funder, who has granted bioRxiv a license to display the preprint in perpetuity. It is made available under a CC-BY-NC-ND 4.0 International license.

tibial nerve and median nerve. Vibratory stimuli were applied to different locations of the hindlimb or forelimb using a calibrated piezo stimulator (Physik Instrumente P-841, E509 controller, E504 amplifier), so that the neural responses to all combinations of locations, frequencies and amplitudes could be characterized. To determine the mechanical sensitive threshold and the frequency tuning of each afferent, a series of sinusoidal mechanical stimuli (duration 20 s for frequencies above 100 Hz; linearly increasing amplitude) were applied to the hand-mapped receptive field of individual afferents with the piezo actuator.

The signal was amplified and filtered (>10 Hz and <10 kHz) and acquired at 30 kHz (PXIe-1073, National Instruments) using WaveSurfer (https://wavesurfer.janelia.org/) MATLAB (Mathworks) routines. Trial start, stimulus onset triggers, and details of stimulus were saved in parallel on separate channels and used for *post-hoc* alignment of recorded spikes. After the recording, animals were euthanized by overdose with isoflurane (5%) followed by cervical dislocation and bleeding.

Vibrotactile stimuli

The vibrotactile stimuli were generated by a bimorph piezoelectric multilayer bender actuator with a piezoelectric stack actuator (P-841.3, Physik Instrumente) equipped with a strain gauge feedback sensor for high frequency stimulations (above 100 Hz). A hand-cut blunt plastic cone was mounted on the actuator. The actuator and sensor controllers (E-662, E-618.1 and E-509.S1, Physik Instrumente) operated in an open loop with a contacting force below 50 mN on the skin of mice. The forces of our vibrotactile stimuli measured at the static states of 3µm, and 30 µm, were less than 10mN, and 10-30 mN. Pure sinusoids (250 or 500 ms duration) of a wide range of frequencies (100 to 1900 Hz) calibrated to produce a desired displacement amplitude (0.01 to 20 µm) were sampled at 10 kHz (USB-6353, National Instruments) and fed to the actuator controller. The sensor measurements were continuously acquired and recalibration of motor commands was regularly performed for the stimuli to remain highly consistent, by comparing the ground truth data acquired optically with a laser doppler vibrometer system (Polytec, OFV-5000). The spectrum of the acquired sensor measurements was analyzed to ensure the integrity of their frequency content (13, 38).

Optogenetic stimuli

Optogenetic stimulation of the parvalbumin neurons in thalamic reticular nucleus (TRN-PV) was generated by blue light illumination (473 nm, 50 mW; Obis LX FP 473, Coherent) out of a fiber (3.5 µm core diameter, 0.045 NA) operated in analog control mode or by yellow light illumination (568 nm, 500 mW; Sapphire LP/LPX, Coherent) fed into an optic fiber with an achromatic FiberPorts (Thorlabs), gated with a shutter. The laser power or the shutter was controlled by analog signals from the WaveSurfer (https://wavesurfer.janelia.org/). For the blue laser, the stimulus was a 40-Hz train of square pulses (2000 ms duration, 1 ms pulse length). For the yellow laser, the stimulus was a continuous square pulses (2000 ms duration). The mean power of the stimulation signal used in our experiments was 1.2 mW for blue and 0.5 mW for yellow (measured at the tip of the fiber).

Fiber-optic implantation in ipsilateral TRN involved cutting an optic fiber (high OH, 400 mm core, 0.39 NA, Thorlabs) with a diamond knife followed by insertion into the 1.25 mm diameter of a ceramic ferrule (Thorlabs) with a 440 mm bore (*50*). The optic fiber was

bioRxiv preprint doi: https://doi.org/10.1101/2023.10.13.562210; this version posted October 17, 2023. The copyright holder for this preprint (which was not certified by peer review) is the author/funder, who has granted bioRxiv a license to display the preprint in perpetuity. It is made available under a CC-BY-NC-ND 4.0 International license.

adhered to the ferrule with epoxy (Gorilla Glue Company). Both ends of the optic fiber were finely ground with sandpaper and grinding puck (Thorlabs). The optic fiber was implanted to thalamic reticular nucleus with a 45° angle laterally. Dental cement (C&B Metabond) was applied to adhere the optic fiber to the surface of the skull. For optical stimulation of Pacinian corpuscles, the stimulus was 20 ms short square pulses with near threshold intensity. Stimulation of different locations on the hindpaw was achieved by manually directing the optical fiber to a 7 × 7 mm area, and the laser beam was focused with FiberPorts (Thorlabs), which focused the light to a 474-μm diameter spot (measured with a beam profiler (Laser Beam profiler Spiricon, SP620U and BeamMic software).

Electrical stimuli

For terminal microstimulation experiments in both S1 and DCN, a craniotomy above the target region was performed and bipolar electrodes (platinum–iridium 250 μm spacing, FHC) were lowered into the contralateral gracile nucleus, or the ipsilateral VPL of the thalamus (coordinates: electrode angled 45°, 2 mm posterior to bregma, 5.5 mm lateral, 5 mm deep) for S1 imaging. For DCN imaging experiments, electrodes were targeted at ipsilateral dorsal horn of lumbar 4 to lumbar 6 spinal cord or the contralateral inferior colliculus (coordinates: 1.5 mm posterior to lambda, at tissue entry, 1.5 mm lateral, 1 mm deep).

For behavioral experiments, the stimulus electrodes were composed of twisted two thin platinum–iridium wires (101R-1W, Science Products) soldered directly to the connector and 1 kHz impedance to <1000 kΩ of the electrodes on average was measured by NanoZ impedance meter (Plexon). With intrinsic imaging data or the known somatotopy, one or two pairs of electrodes were implanted to the center of the hindlimb representation of left S1 (200–300 μm) or right posterior gracile nucleus (angled 45° rostrally, 100–200 μm), and the brain was covered by first Kwik-Sil silicone elastomer (World Precision Instruments), cyanoacrylate glue and dental acrylic.

The stimulus was generally a train of square pulses (500 ms duration, 0.1-0.3 ms pulse length) with various frequencies (10 to 1000 Hz) and amplitudes (100–300 μA). Validation of microstimulation was also tested by stimulus evoked responses in calcium imaging in S1 or by local field potential recording in the projected areas after weeks of implantation and stimulation. For example, electrical stimulation in the gracile nucleus was verified by recording the stimulus evoked field potential from contralateral S1.

Neurectomy

The surgery was performed in mice under isoflurane anesthesia (1.5–2%) and additional analgesic (0.1 mg/kg buprenorphine i.m.), local anesthetic (30 μl 1% lidocaine s.c. in the hindlimb) and anti-inflammatory drugs (2.5 mg/kg dexamethasone i.m. and 5 mg/kg carprofen s.c.) were administered. The hair of the forelimb was shaved and a skin incision was made behind the knee. The muscles and connective tissues were retracted to expose the tibial nerves innervating the interosseous region. Complete transection of the nerve branch innervating the group of Pacinian corpuscles on the fibula was performed. After suturing the skin, mice were allowed to recover for 3 days before any follow-up experiments. The electrophysiological experiment was performed 1 month after surgery and the animals were euthanized. During some terminal nerve fiber recording experiments, the same procedure was performed at the end of the recording, to observe

bioRxiv preprint doi: https://doi.org/10.1101/2023.10.13.562210; this version posted October 17, 2023. The copyright holder for this preprint (which was not certified by peer review) is the author/funder, who has granted bioRxiv a license to display the preprint in perpetuity. It is made available under a CC-BY-NC-ND 4.0 International license.

the immediate effects of neurectomy on different fiber types responding to vibration or touch.

Histology

Upon completion of terminal experiments, isoflurane was raised to 5% and 0.2 ml pentobarbital was delivered through an intraperitoneal injection. The animal was transcardially perfused with 20 ml of 0.9% NaCl and then 50 ml of 4% paraformaldehyde in 0.1 M PB. The brain or body parts were removed and placed in 4% PFA overnight. A vibratome (Leica VT1200S) was used to cut tangential or coronal sections (100 µm thick). Slices were washed three times using 1X PBS, then mounted to a slide using SlowFade Gold (Thermofisher Scientific) or Mounting Medium With DAPI (Ancam,104139) for imaging using a fluorescence microscope (Olympus BX53) or confocal microscopy (ZEISS LSM 800). In most of the recording in the deep brain areas, the electrode was coated with DiI (ThermoFisher) before insertion, for identification of the precise recording site.

Confocal imaging

Dissection of tissue was done under a fluorescent microscope (Leica M165FC). The expression pattern of GCaMP, ArchT or ChR2 was imaged by illuminating the dissected tissue with a blue LED light, with emission channels optimized for each fluorophore (GFP, or YFP), and subsequently imaged with confocal or two-photon microscopes. Confocal imaging was done using a ZEISS LSM 800 confocal microscope. Images were acquired using 405, 488, and 561 nm laser lines with emission channels optimized for each fluorophore (DAPI, GFP, DiI) while minimizing cross-talk between channels. Images were acquired at 512×512 with sampling resolution ranging from 0.15 to 1 µm per pixel. Z-stacks were acquired using 0.5 to 5 µm steps and the confocal pinhole was set to 1 AU. Colocalization was performed manually. The imaging data was analyzed using ImageJ (NIH).

Data analysis

Significant responses

For calcium imaging, ROIs were circular or drawn manually for the targeted neuronal structures in ImageJ (NIH). Fluorescence time-courses were computed as the mean of all pixels within the ROI at each time point, then extracted using Miji (*51*), and finally synchronized with the stimulation. Evoked responses were computed as changes in fluorescence relative to baseline fluorescence. Frequency selectivity for individual neurons or nerve fibers was quantified by a previously reported method (*52*). To computing tuning properties, the fluorescence signal was calculated as $\Delta f/f=(f-f0)/f0$, where f0 is the baseline fluorescence signal averaged over the 1 s period immediately before the start of the vibration stimulation and f is the fluorescence signal averaged over the first 1.5 s period after the start of the stimulation. Tuning curves were obtained by calculating the mean fluorescence signal ($\Delta f/f$) for each stimulation, and then fitting a polynomial curve to the resulting data. For electrophysiological recording, tuning curves were computed by the spike rate of the neurons.

bioRxiv preprint doi: https://doi.org/10.1101/2023.10.13.562210; this version posted October 17, 2023. The copyright holder for this preprint (which was not certified by peer review) is the author/funder, who has granted bioRxiv a license to display the preprint in perpetuity. It is made available under a CC-BY-NC-ND 4.0 International license.

Tuning curve fitting

Neuronal structures were considered to be responsive if the maximum stimulus-related fluorescence response (Δf/f) to any stimulus was greater than 5% on average, and also greater than 2 standard deviations (SD) above the mean baseline fluorescence. In addition, we required that neurons responded at least 2 SD above baseline on at least 20% of the trials tested. The same criteria were used to identify neurons with significant responses to the vibration, optogenetic and electrical stimuli.

Neuronal structures were considered to be frequency selective if they were responsive and also met the following criteria: (1) well fit by the polynomial function ($r > 0.7$, $p < 0.05$), and (2) tuning index (TI) > 0.2

$$TI = \frac{\mu_{pref} - \mu_{ortho}}{\mu_{pref} + \mu_{ortho}},$$

where μ_{pref} denotes the mean response to the preferred stimulus frequency and μ_{ortho} is the mean response to the least preferred stimulus frequency, defined by the curve fitting. To characterize a neuron's tuning to vibration frequency, the normalized mean responses were fit to frequency by the polynomial curve fitting function (MATLAB) using the method of non-linear least squares, with the degree of polynomial fit set at 6. The tuning preference of individual neurons was defined by the peak of the curve and the tuning width was defined by the half-width at the half-maximum of the curve (HWHM).

Phase-locked spiking

To determine whether a nerve fiber or a neuron was entrained by the sinusoidal vibration, we calculated standardized inter-spike intervals. We chose this measure because it is immune to variability in response onset times across different stimulus repetitions. For a given vibration frequency, the inter-spike intervals (ISI) of all possible spike pairs that occurred during stimulation were calculated and grouped across stimulus repetitions. Because entrained spiking should yield an ISI distribution that peaks at integer multiples of the sinusoidal stimulus period T, values were converted to standardized inter-spike intervals (SISI) according to SISI = T + (ISI − nT), where nT is the integer multiple of T closest to ISI. Entrainment probability was defined as the percentage of ISIs in the [$nT - T/12$, $nT + T/12$] interval. Given that standardized ISIs are distributed between $nT - T/2$ and $nT + T/2$, entrainment probability should equal unity in the case of perfect entrainment and be equal to 1/6 in the case of chance entrainment. For each neuron and at each frequency we repeated the calculation of entrainment probability 1,999 times with randomly sampled ISIs (with replacement). We then measured whether the lower 99th percentile of the repeated measures was less than 1/6, which constitutes a one-tailed bootstrap test at significance level $P < 0.01$.

Temporal and rate coding index

Temporal coding index (TCI) and rate coding index (RCI) were computed for individual imaged neurons in S1 or in DCN by comparing their tuning curves to vibrotactile stimuli and electrical microstimulation of downstream brain areas. Temporal coding index (TCI) was defined as the reproducibility of the vibration-induced frequency tuning curve by temporally structured microstimulation, which mimics the spikings of the sensory afferents responding to vibration on the skin. TCI was defined as the correlation

bioRxiv preprint doi: https://doi.org/10.1101/2023.10.13.562210; this version posted October 17, 2023. The copyright holder for this preprint (which was not certified by peer review) is the author/funder, who has granted bioRxiv a license to display the preprint in perpetuity. It is made available under a CC-BY-NC-ND 4.0 International license.

coefficient between tuning curves to vibration vs. microstimulation. On the other hand, rate coding index (RCI) was defined as the invariant responses from the microstimulation with various frequencies but with the same number of electrical pulses, which mimics the fixed number of spikings of the presynaptic inputs. In the case, where the temporal precision is not critical and the response to the stimulation is only determined by the number of spikes, the neural responses of the postsynaptic neuron should be the same for all stimulation with different frequencies under the control of the inputs' spiking rate.

$$RCI = 1 - \frac{max\,(Res) - mean\,(Res)}{max\,(Res) + mean\,(Res)}$$

where *Res* denotes the responses to all four microstimulation patterns with different frequencies (30, 100, 300 Hz and 100 Hz jittered by ±3 ms, from a uniform distribution) but with the same number of 15 pulses.

Statistics

No statistical methods were used to predetermine sample size and all experimental animals were included in the analysis. The normality assumption was tested with the Kolmogorov-Smirnov test. Non-parametric tests were used when the normality assumption was not met. We used a two sided non-parametric Wilcoxon rank-sum test to compare two groups and the Kruskal–Wallis test to compare multiple groups with *post-hoc* tests using Dunn's test, without assumptions of normality or equal variances. Paired-sample t-test was used to compare the effect of optogenetic manipulations. Pearson's correlation coefficient was applied to the analysis related to frequency tuning. All statistical methods were two-sided. All data analyses were performed with custom written routines in MATLAB.

Microstimulation frequency discrimination behavioral task

Seven mice were prepared for a microstimulation frequency discrimination task by fixing a custom-made titanium head bar to the skull with a cyanoacrylate adhesive (ergo 5011, IBZ Industrie) and dental cement, and implanting the stimulating electrodes in the hindlimb region of the DCN and S1, under general isoflurane anesthesia (1.5–2%). After surgical recovery, mice were placed under a water restriction regime (1ml/day) and habituated to the tunnel and head-fixation frame where they performed the task.

Mice were trained daily to discriminate microstimulation at lower frequencies from stimuli at higher frequencies in a two-alternative forced-choice (2AFC) task. Each trial began with a 1-s hold period in which mice had to refrain from licking the reward ports. Licking of the reward ports resulted in resetting the 1-s interval. After the holding period, a 0.5 s stimulus was delivered to the DCN or S1, which consisted of 0.2 ms square pulses of 50 Hz, 100 Hz, or 300 Hz and amplitudes of 40-360 μA. A 2-s response window followed the stimulus presentation in which mice were trained to initiate licking of the left water port in response to lower frequencies and to the right water port in response to higher frequencies. To minimize a direction bias, the trial type was chosen pseudo-randomly by allowing a maximum of two trials of the same type in a row. Hit trials (correctly licking left for lower frequencies and right for higher frequencies) were rewarded by a drop of water and the immediate transition to a new trial. Miss trials (licks to the incorrect side) resulted in a timeout punishment of 2-4 seconds. If mice did not lick within the 2-s

bioRxiv preprint doi: https://doi.org/10.1101/2023.10.13.562210; this version posted October 17, 2023. The copyright holder for this preprint (which was not certified by peer review) is the author/funder, who has granted bioRxiv a license to display the preprint in perpetuity. It is made available under a CC-BY-NC-ND 4.0 International license.

response window this resulted in a 2-s timeout. After the timeout period a new trial started with the hold period in which mice had to refrain from licking for 1-s. Mice were trained for 5-14 days using the outermost frequencies later used for testing, 50 Hz and 300 Hz, which was shifted to the restricted test frequencies of 50 Hz and 100 Hz or 100 Hz and 300 Hz, with 100 Hz treated as the center standard frequency. Testing began, when mice reached sensitivity performance of d' > 1 over 100 trials. D-prime values were calculated as d' = z(hit rate) - z(miss rate), where z(*p*) is the inverse of the cumulative Gaussian distribution function.

The behavioral task was programmed and controlled with the Bpod real-time system (Sanworks). Behavioral data were analyzed in MATLAB and R (R statistical computing).

Focused ion beam scanning electron microscopy (FIB-SEM)

Animals were anesthetized with sodium pentobarbital (60 mg/kg) by intraperitoneal injection. They were subsequently transcardially perfused with 15 ml of 0.1M sodium phosphate buffer pH 7.4 and then 60 ml of 2% paraformaldehyde (15710-S, Electron Microscopy Sciences) 1% glutaraldehyde (G7526, Sigma-Aldrich) in 0.1M sodium phosphate buffer pH 7.4. The animals were left for two hours and then the DCN and thalamus were dissected and post-fixed overnight at 4°C in 2% paraformaldehyde 1% glutaraldehyde in 0.1M sodium phosphate buffer pH 7.4. They were then prepared for focused ion beam scanning electron microscopy.

Sample preparation

After overnight post-fixation the samples were prepared for FIB-SEM with support from Pilar Ruga Fahy at the PFMU Electron Microscopy Facility at the University of Geneva. The sample preparation was based on the protocol for preparation of biological specimens for serial block face scanning electron microscopy by Ellisman (*53, 54*). The serial sections were thoroughly rinsed (5 x 3 minutes) in 0.15M cacodylate buffer with 2mM $CaCl_2$ and then postfixed in 4% osmium tetroxide with 3% potassium ferrocyanide for an hour on ice, followed by 20 minutes in 1% thiocarbohydrazide at room temperature and then 30 minutes in 2% osmium tetroxide. In between each solution the samples were thoroughly washed with ddH_2O (5 x 3 minutes). The samples were left overnight in 1% uranyl acetate at 4°C. The next morning the samples were rinsed again (ddH_2O, 5 x 3 minutes) and subsequently incubated in lead aspartate (0.132 g NiPb/ 20 mL aspartic acid, adjusted to pH 5.5 with 1N KOH) at 60°C. The samples were rinsed (ddH_2O, 5 x 3 minutes) a final time before being dehydrated through increased concentrations of ethanol (30%, 50%, 70%, 90% for 7 minutes each; 2 x 100% for 30 minutes each) and then embedded in epoxy embedding medium kit (Epon substitute embedding medium kit; 45359, Sigma Aldrich). For this, the samples were left in 100% propylene oxide for 10 minutes, 25% epoxy resin 75% propylene for 30 minutes, 50% epoxy resin 50% propylene for 30 minutes, 100% epoxy resin for 30 minutes and finally 100% epoxy resin overnight. The samples were then left to harden for 48 hours in a 65°C oven.

Imaging

Imaging was carried out by Iryna Nikonenko from the Electron Microscopy Facility (PFMU) at the University of Geneva (Switzerland) on a Helios 660 Nanolab Dual Beam (FEI) using the Auto Slice and View (ASV 4.2) software. The resin block was trimmed

bioRxiv preprint doi: https://doi.org/10.1101/2023.10.13.562210; this version posted October 17, 2023. The copyright holder for this preprint (which was not certified by peer review) is the author/funder, who has granted bioRxiv a license to display the preprint in perpetuity. It is made available under a CC-BY-NC-ND 4.0 International license.

down to the area of interest with a glass knife and mounted on stub pins. Semi-thin (200 nm) sections were cut on the ultramicrotome and stained with toluidine blue to confirm the region of interest. The samples were coated in 20 nm of gold. For the imaging, an acceleration voltage of 2 kV was used with a current of 0.4 nA. The ion beam was set to an acceleration voltage of 30 kV with a current of 0.79 nA. The DCN sample was imaged at a pixel size of 4 nm and slice thickness of 10 nm. The field of view was 25 by 18 µm and a total stack of 1684 slices was acquired. The thalamus sample was imaged at a pixel size of 6 nm and slice thickness of 10 nm. The field of view was 36 by 28 µm and a total of 600 slices were acquired.

Image alignment and segmentation

The TrakEM2 extension of Fiji (www.fiji.sc) was used to align the images acquired. The stack was then imported into the software Amira (Thermo Fisher Scientific), where the reconstructions were carried out. The different structures - synapses and vesicles - were manually segmented and labeled in the Segmentation workspace. Only synapses with large pre-synaptic elements (at least 2 µm, multiple mitochondria, often multiple synaptic contacts) that have a higher likelihood of being driver synapses were included in the study. The final reconstructions were rendered in the Project workspace using the “interactive thresholding” and “generate surface” tools. Surface area and volume were calculated from the generated surfaces using the “Surface area Volume” tool.

References and Notes

1. E. D. Adrian, K. Umrath, The impulse discharge from the pacinian corpuscle. J. Physiol. 68, 139–154 (1929).
2. V. B. Mountcastle, R. H. LaMotte, G. Carli, Detection thresholds for stimuli in humans and monkeys: comparison with threshold events in mechanoreceptive afferent nerve fibers innervating the monkey hand. J. Neurophysiol. 35, 122–136 (1972).
3. B. D. Gynther, R. M. Vickery, M. J. Rowe, Transmission characteristics for the 1:1 linkage between slowly adapting type II fibers and their cuneate target neurons in cat. Exp. Brain Res. 105, 67–75 (1995).
4. M. J. Rowe, Synaptic transmission between single tactile and kinaesthetic sensory nerve fibers and their central target neurones. Behav. Brain Res. 135, 197–212 (2002).
5. V. Sahai, D. A. Mahns, L. Robinson, N. M. Perkins, G. T. Coleman, M. J. Rowe, Processing of vibrotactile inputs from hairy skin by neurons of the dorsal column nuclei in the cat. J. Neurophysiol. 95, 1451–1464 (2006).
6. P. Herron, R. Dykes, The ventroposterior inferior nucleus in the thalamus of cats: a relay nucleus in the Pacinian pathway to somatosensory cortex. J. Neurophysiol. 56, 1475–1497 (1986).
7. Y. Vázquez, E. Salinas, R. Romo, Transformation of the neural code for tactile detection from thalamus to cortex. Proc. Natl. Acad. Sci. U. S. A. 110, E2635–44 (2013).

bioRxiv preprint doi: https://doi.org/10.1101/2023.10.13.562210; this version posted October 17, 2023. The copyright holder for this preprint (which was not certified by peer review) is the author/funder, who has granted bioRxiv a license to display the preprint in perpetuity. It is made available under a CC-BY-NC-ND 4.0 International license.

8. A. K. Suresh, H. P. Saal, S. J. Bensmaia, Edge orientation signals in tactile afferents of macaques. J. Neurophysiol. 116, 2647–2655 (2016).

9. H. P. Saal, M. A. Harvey, S. J. Bensmaia, Rate and timing of cortical responses driven by separate sensory channels. Elife. 4, e10450 (2015).

10. I. Birznieks, S. McIntyre, H. M. Nilsson, S. S. Nagi, V. G. Macefield, D. A. Mahns, R. M. Vickery, Tactile sensory channels over-ruled by frequency decoding system that utilizes spike pattern regardless of receptor type. Elife. 8 (2019), doi:10.7554/eLife.46510.

11. I. Birznieks, R. M. Vickery, Spike Timing Matters in Novel Neuronal Code Involved in Vibrotactile Frequency Perception. Curr. Biol. 27, 1485–1490.e2 (2017).

12. E. Salinas, A. Hernandez, A. Zainos, R. Romo, Periodicity and firing rate as candidate neural codes for the frequency of vibrotactile stimuli. J. Neurosci. 20, 5503–5515 (2000).

13. M. Prsa, K. Morandell, G. Cuenu, D. Huber, Feature-selective encoding of substrate vibrations in the forelimb somatosensory cortex. Nature. 567, 384–388 (2019).

14. L.-G. Wu, T. A. Ryan, L. Lagnado, Modes of vesicle retrieval at ribbon synapses, calyx-type synapses, and small central synapses. J. Neurosci. 27, 11793–11802 (2007).

15. D. Lenzi, J. W. Runyeon, J. Crum, M. H. Ellisman, W. M. Roberts, Synaptic vesicle populations in saccular hair cells reconstructed by electron tomography. J. Neurosci. 19, 119–132 (1999).

16. J.-Y. Sun, X.-S. Wu, L.-G. Wu, Single and multiple vesicle fusion induce different rates of endocytosis at a central synapse. Nature. 417, 555–559 (2002).

17. S. M. Sherman, R. W. Guillery, On the actions that one nerve cell can have on another: Distinguishing “drivers” from “modulators.” Proceedings of the National Academy of Sciences. 95, 7121–7126 (1998).

18. N. Yamawaki, M. G. Raineri Tapies, A. Stults, G. A. Smith, G. M. Shepherd, Circuit organization of the excitatory sensorimotor loop through hand/forelimb S1 and M1. Elife. 10 (2021), doi:10.7554/eLife.66836.

19. S. Temereanca, D. J. Simons, Functional topography of corticothalamic feedback enhances thalamic spatial response tuning in the somatosensory whisker/barrel system. Neuron. 41, 639–651 (2004).

20. F. Briggs, W. M. Usrey, Corticogeniculate feedback and visual processing in the primate. J. Physiol. 589, 33–40 (2011).

21. D. Pinault, M. Deschênes, Anatomical evidence for a mechanism of lateral inhibition in the rat thalamus. Eur. J. Neurosci. 10, 3462–3469 (1998).

22. Y.-T. Li, L. A. Ibrahim, B.-H. Liu, L. I. Zhang, H. W. Tao, Linear transformation of thalamocortical input by intracortical excitation. Nat. Neurosci. 16, 1324–1330 (2013).

bioRxiv preprint doi: https://doi.org/10.1101/2023.10.13.562210; this version posted October 17, 2023. The copyright holder for this preprint (which was not certified by peer review) is the author/funder, who has granted bioRxiv a license to display the preprint in perpetuity. It is made available under a CC-BY-NC-ND 4.0 International license.

23. S.-H. Lee, A. C. Kwan, S. Zhang, V. Phoumthipphavong, J. G. Flannery, S. C. Masmanidis, H. Taniguchi, Z. J. Huang, F. Zhang, E. S. Boyden, K. Deisseroth, Y. Dan, Activation of specific interneurons improves V1 feature selectivity and visual perception. Nature. 488, 379–383 (2012).

24. G. Rankin, A. M. Chirila, A. J. Emanuel, Z. Zhang, C. J. Woolf, J. Drugowitsch, D. D. Ginty, Nerve injury disrupts temporal processing in the spinal cord dorsal horn through alterations in PV+ interneurons. bioRxiv (2023), p. 2023.03.20.533541.

25. R. I. Martinez-Garcia, B. Voelcker, J. B. Zaltsman, S. L. Patrick, T. R. Stevens, B. W. Connors, S. J. Cruikshank, Publisher Correction: Two dynamically distinct circuits drive inhibition in the sensory thalamus. Nature. 585, E13 (2020).

26. Y. Li, V. G. Lopez-Huerta, X. Adiconis, K. Levandowski, S. Choi, S. K. Simmons, M. A. Arias-Garcia, B. Guo, A. Y. Yao, T. R. Blosser, R. D. Wimmer, T. Aida, A. Atamian, T. Naik, X. Sun, D. Bi, D. Malhotra, C. C. Hession, R. Shema, M. Gomes, T. Li, E. Hwang, A. Krol, M. Kowalczyk, J. Peça, G. Pan, M. M. Halassa, J. Z. Levin, Z. Fu, G. Feng, Distinct subnetworks of the thalamic reticular nucleus. Nature. 583, 819–824 (2020).

27. Y.-T. Li, W.-P. Ma, L.-Y. Li, L. A. Ibrahim, S.-Z. Wang, H. W. Tao, Broadening of inhibitory tuning underlies contrast-dependent sharpening of orientation selectivity in mouse visual cortex. J. Neurosci. 32, 16466–16477 (2012).

28. S. N. Flesher, J. L. Collinger, S. T. Foldes, J. M. Weiss, J. E. Downey, E. C. Tyler-Kabara, S. J. Bensmaia, A. B. Schwartz, M. L. Boninger, R. A. Gaunt, Intracortical microstimulation of human somatosensory cortex. Sci. Transl. Med. 8, 361ra141 (2016).

29. K. C. Stieger, J. R. Eles, K. A. Ludwig, T. D. Y. Kozai, Intracortical microstimulation pulse waveform and frequency recruits distinct spatiotemporal patterns of cortical neuron and neuropil activation. J. Neural Eng. 19 (2022), doi:10.1088/1741-2552/ac5bf5.

30. R. Romo, A. Hernández, A. Zainos, E. Salinas, Somatosensory discrimination based on cortical microstimulation. Nature. 392, 387–390 (1998).

31. T. Callier, N. W. Brantly, A. Caravelli, S. J. Bensmaia, The frequency of cortical microstimulation shapes artificial touch. Proc. Natl. Acad. Sci. U. S. A. 117, 1191–1200 (2020).

32. G. M. G. Shepherd, N. Yamawaki, Untangling the cortico-thalamo-cortical loop: cellular pieces of a knotty circuit puzzle. Nat. Rev. Neurosci. 22, 389–406 (2021).

33. M. M. Halassa, L. Acsády, Thalamic Inhibition: Diverse Sources, Diverse Scales. Trends Neurosci. 39, 680–693 (2016).

34. G. Born, F. A. Schneider-Soupiadis, S. Erisken, A. Vaiceliunaite, C. L. Lao, M. H. Mobarhan, M. A. Spacek, G. T. Einevoll, L. Busse, Corticothalamic feedback sculpts visual spatial integration in mouse thalamus. Nat. Neurosci. 24, 1711–1720 (2021).

bioRxiv preprint doi: https://doi.org/10.1101/2023.10.13.562210; this version posted October 17, 2023. The copyright holder for this preprint (which was not certified by peer review) is the author/funder, who has granted bioRxiv a license to display the preprint in perpetuity. It is made available under a CC-BY-NC-ND 4.0 International license.

35. M. A. Castro-Alamancos, Properties of primary sensory (lemniscal) synapses in the ventrobasal thalamus and the relay of high-frequency sensory inputs. J. Neurophysiol. 87, 946–953 (2002).

36. C. Mo, I. Petrof, A. N. Viaene, S. M. Sherman, Synaptic properties of the lemniscal and paralemniscal pathways to the mouse somatosensory thalamus. Proc. Natl. Acad. Sci. U. S. A. 114, E6212–E6221 (2017).

37. P. Lavallée, M. Deschênes, Dendroarchitecture and lateral inhibition in thalamic barreloids. J. Neurosci. 24, 6098–6105 (2004).

38. K.-S. Lee, D. de Thomas Wagner, M. Sanders, D. Huber, Emergence of a somatosensory tonotopic map for substrate vibration in the brainstem. bioRxiv (2023), p. 2023.09.26.559502.

39. H. Adesnik, L. Abdeladim, Probing neural codes with two-photon holographic optogenetics. Nat. Neurosci. 24, 1356–1366 (2021).

40. L. Carrillo-Reid, S. Han, W. Yang, A. Akrouh, R. Yuste, Controlling Visually Guided Behavior by Holographic Recalling of Cortical Ensembles. Cell. 178, 447–457.e5 (2019).

41. D. Lee, J. H. Hyun, K. Jung, P. Hannan, H.-B. Kwon, A calcium- and light-gated switch to induce gene expression in activated neurons. Nat. Biotechnol. 35, 858–863 (2017).

42. L. Gao, K. Kostlan, Y. Wang, X. Wang, Distinct Subthreshold Mechanisms Underlying Rate-Coding Principles in Primate Auditory Cortex. Neuron. 91, 905–919 (2016).

43. P. Reinagel, R. C. Reid, Temporal coding of visual information in the thalamus. J. Neurosci. 20, 5392–5400 (2000).

44. R. M. Vickery, K. K. W. Ng, J. R. Potas, M. N. Shivdasani, S. McIntyre, S. S. Nagi, I. Birznieks, Tapping Into the Language of Touch: Using Non-invasive Stimulation to Specify Tactile Afferent Firing Patterns. Front. Neurosci. 14, 500 (2020).

45. A. J. Loutit, M. N. Shivdasani, T. Maddess, S. J. Redmond, J. W. Morley, G. J. Stuart, I. Birznieks, R. M. Vickery, J. R. Potas, Peripheral Nerve Activation Evokes Machine-Learnable Signals in the Dorsal Column Nuclei. Front. Syst. Neurosci. 13, 11 (2019).

46. T.-W. Chen, T. J. Wardill, Y. Sun, S. R. Pulver, S. L. Renninger, A. Baohan, E. R. Schreiter, R. A. Kerr, M. B. Orger, V. Jayaraman, L. L. Looger, K. Svoboda, D. S. Kim, Ultrasensitive fluorescent proteins for imaging neuronal activity. Nature. 499, 295–300 (2013).

47. J. B. Wekselblatt, E. D. Flister, D. M. Piscopo, C. M. Niell, Large-scale imaging of cortical dynamics during sensory perception and behavior. J. Neurophysiol. 115, 2852–2866 (2016).

48. C. Chen, J. Zhang, L. Sun, Y. Zhang, W.-B. Gan, P. Tang, G. Yang, Long-term imaging of dorsal root ganglia in awake behaving mice. Nat. Commun. 10, 3087 (2019).

bioRxiv preprint doi: https://doi.org/10.1101/2023.10.13.562210; this version posted October 17, 2023. The copyright holder for this preprint (which was not certified by peer review) is the author/funder, who has granted bioRxiv a license to display the preprint in perpetuity. It is made available under a CC-BY-NC-ND 4.0 International license.

49. M. Pachitariu, C. Stringer, K. D. Harris, Robustness of Spike Deconvolution for Neuronal Calcium Imaging. J. Neurosci. 38, 7976–7985 (2018).

50. K.-S. Lee, K. Vandemark, D. Mezey, N. Shultz, D. Fitzpatrick, Functional Synaptic Architecture of Callosal Inputs in Mouse Primary Visual Cortex. Neuron. 101, 421–428.e5 (2019).

51. D. Sage, D. Prodanov, J. Tinevez, J. Schindelin, M. I. J. Year, Making Interoperability Between ImageJ and Matlab Possible. ImageJ User & Developer.

52. K.-S. Lee, X. Huang, D. Fitzpatrick, Topology of ON and OFF inputs in visual cortex enables an invariant columnar architecture. Nature. 533, 90–94 (2016).

53. T. J. Deerinck, E. A. Bushong, M. H. Ellisman, A. Thor, Preparation of biological tissues for serial block face scanning electron microscopy (SBEM) (2022) (available at https://slack.protocols.io:8443/view/preparation-of-biological-tissues-for-serial-block-b65drg26.html).

54. C. Georgiou, V. Kehayas, K. S. Lee, F. Brandalise, D. A. Sahlender, J. Blanc, G. Knott, A. Holtmaat, A subpopulation of cortical VIP-expressing interneurons with highly dynamic spines. Commun Biol. 5, 352 (2022).

Acknowledgments

We thank A. Taylor and J. Marozeau for advice and comments on the manuscript; G. Cuenu for help with histological techniques; R. Vickery for advice on electrophysiology experiments; P. Ruga Fahy for assistance with FIB-SEM sample preparation and I. Nikonenko for FIB-SEM imaging; and G. Cuenu for help with breeding mice. **Funding:** This work was supported by the Swiss National Science Foundation (310030_184829), the European Research Council (OPTOMOT), and the International Foundation for Research in Paraplegia. K.-S.L. is a EMBO Postdoctoral Fellow (ALTF_816-2020). **Author contributions:** Conceptualization: K.-S.L., M.P. and D.H. Methodology: K.-S.L., M.P. and D.H. Investigation: K.-S.L., A.L., M.S. and D.T.W. Visualization: K.-S.L., A.L. and D.T.W. Funding acquisition: K.-S.L. and D.H. Supervision: K.-S.L. and D.H. Writing – original draft: K.-S.L. Writing – review & editing: A.L., D.T.W. and D.H. **Competing interests:** The authors declare no competing interests. **Data and materials availability:** All data analyzed and all custom Matlab code used for the analysis in the current study will be available upon publication from the corresponding author upon reasonable request.